Modeling micro-cracking and failure in short fiber-reinforced composites

G. Lancioni[a,*], R. Alessi[b]

[a] *Dipartimento di Ingegneria Civile, Edile e Architettura, Università Politecnica delle Marche, Via Brecce Bianche 1, 60131 Ancona, Italy, http://www.univpm.it/giovanni.lancioni*

[b] *Dipartimento di Ingegneria Civile e Industriale, Università di Pisa, Largo Lucio Lazzarino, 56122 Pisa, Italy*

Abstract

Composites made of reinforcing short fibers embedded into brittle matrices, like, e.g., fiber-reinforced concretes, exhibit enhanced strength and ductility properties. Their failure process induced by tensile loadings involves hardening and softening stages as a result of matrix multiple micro-cracking, due to stress bridging of fibers across matrix micro-cracks, and strain localization phenomena.

In the present paper, a variational model is proposed for the description of the intriguing failure mechanisms observed in short fibre-reinforced composites subjected to tensile loadings. The key modeling idea is to schematize the composite as a mixture of two phases, a brittle phase, representative of the matrix, and a ductile phase, accounting for the fibers reinforcement, which are coupled by elastic bonds.

Different modeling levels of increasing complexity are proposed, ranging from a simplified one-dimensional analytical model to a three-dimensional variational model. Within the variational formulation, specific damage and plastic energies are assigned to the two phases, incorporating non-local gradient terms, and governing equations and evolution laws for the internal variables, as yield inequalities, consistency conditions and normality rules, are deduced from minimum principles. Parameters calibration is discussed as well as the importance of three internal lengths incorporated into the model. Moreover, the variational structure of the problem allow for a straightforward finite element implementation based on an incremental energy minimization algorithm and several aspects of the response are highlighted by means of numerical examples.

Keywords: Variational fracture, gradient plasticity, fiber-reinforced concrete, ductile failure, micro-cracking

Contents

*Corresponding Author

Email addresses: g.lancioni@univpm.it (G. Lancioni), roberto.alessi@unipi.it (R. Alessi)

1. Introduction

High-performance applications in structural engineering continuously demand for innovative materials with enhanced mechanical properties. One way to meet this request is to develop composites where different materials with specific properties are combined to achieve the desired performances. Among the many typologies of composites, we focus on short fiber-reinforced composites, which are obtained by embedding fibers of short length within matrices to improve their mechanical properties, [1, 2, 3, 4]. In construction engineering, an example is given by ultra-high performance fibre-reinforced concretes (UHPFRC), in which tensile strength, ductility, and durability are significantly improved by adding great amounts of short fibres ($> 2\%$ by volume), usually made of steel, within ultra high strength cementitious matrices [5]. Many experimental studies on UHPFRC have been conducted [6, 7, 8], highlighting the role of mix design [9], and proposing recommendations for a correct use in structural applications [10].

The response of UHPFRC to tensile loads clearly shows the advantage of fibers on the overall performances of the composite, and it is taken as an explicative example of the peculiar mechanical behaviour of short fiber-reinforced composites. Three different stages distinguish the tensile response of UHPFRC, as shown in Fig. 1. The initial stage is linear elastic. Then a non-linear stress-hardening response follows, characterized by a process of matrix micro-cracking. This stage, totally absent in ordinary concretes, is due to the bridging action of fibers, transferring stresses across micro-cracks, which progressively open within the whole bar. After the peak-stress has been reached, no further cracks develop, and the response becomes stress-softening, with strain localization within a single crack, leading to the fully failure. In case of sufficiently long bars, the softening response may not be observed, since an unstable response (snap-back) leads to abrupt failure [11]. During the failure process both damage and plastic strains develop, as shown by unloading curves [8, 12], which exhibit reduction of the elastic modulus and presence of permanent deformations.

Processes of micro- and multi-cracking are observed in many other cases, as, for instance, in hybrid composites [13], in coatings [14], in thin films on rigid substrates [15], in flexible electronic devices [16], in mud and clay desiccation processes [17] and even in the crocodile skin [18]. The correct description of the complex multi-cracks patterning is of fundamental importance when assessing material durability and ductility [19]. Its accurate characterization, as the knowledge of the micro-crack spacing, can also allow for novel and advanced applications as auto-diagnostic materials and visual overload strain sensors [20].

In this work, a variational model is proposed, able to describe the intriguing tensile failure of short fiber-reinforced composites, where rupture is anticipated by a stress-hardening process of multi-cracking, and special attention is payed to the characterization of the dissipation mechanisms induced by damage and plastic strain evolution.

The model is developed within the framework of energetic formulations for rate-independent systems [21, 22, 23], which have been applied to the modelling of many problems of non-smooth evolution and material instability induced by strain localization. Among the many works available in literature, we mention the phase-field models for brittle fracture [24, 25, 26], quasi-brittle fracture [27], cohesive fracture, [28, 29, 30], anisotropic fracture [31, 32], plastic shear bands and ductile fracture [33, 34, 35, 36], phase-transformation [37, 38]. According to the energetic approach, once the internal energy density of the material is specified, the entire evolution is governed by three energetic requirements, which are the stability criterion, the energy balance and the dissipation inequality. Compared to standard theories, the energetic formulation owns the advantage of being completely derivative-free, admitting discontinuities both in space and in time. Such a feature, in addition to evolution governing principles, allows for a natural and straightforward numerical implementation based on incremental energy minimization schemes, which is a valuable alternative to the integration of differential evolution equations [39, 22].

A first variational model for the description of stress-hardening and stress-softening stages of micro-cracking and macro-crack opening, as observed in tensile UHPFRC, has been proposed in [40]. By introducing an internal damage variable within the model, the micro-cracking process is described by zones of diffuse damage, where single micro-cracks are indistinguishable, and the final macro-crack is reproduced by damage localization. The model accurately captures the tensile stress-strain response found in tensile experiments on UHPFRC, but it is unable to predict the patterning of multiple cracks, as well as the crack spacing, which is a key aspect when assessing durability. Furthermore, the model does not describe plastic strain evolution and, therefore, it does not correctly predict dissipation and ductility.

The modeling of complex multiple cracks patterning is still an open issue. In the one-dimensional context, it is proved that rate-independent formulations based on a single displacement field are not able to describe multiple strain localizations [41]. In phase-field models [42, 40], damage diffuses in regime of stress-hardening, and it localizes in a single region in regime of stress-softening. A similar behaviour is observed in non-local plasticity models [41, 43, 33]. In [37, 38], the localized zone of phase transformation extends instead of promoting the formation of new localization areas. Models with multiple internal variable, as damage and plasticity [35], are also unable to describe the occurrence of multiple zones of localization.

On the contrary, phenomena of fragmentation and multiple strain localization have been reproduced by phase-field models of thin films on rigid substrates [44] and hybrid composites [45]. In both the cases, the interface between layers has played a key role in the description of multiple cracks. Inspired by these studies, we propose a model based on the concept of superposition of continua [46]. The body is assumed to be a mixture of two solid phases representing the matrix and the fiber reinforcement. Phases are weighted by suitable volume fractions, and they are coupled by linear elastic springs, which play the role of transferring stresses among phases, thus accounting for the fibre-bridging effect. The matrix is assumed to be brittle, and it is described by a variational phase-field damage model [25], where a damage internal variable describes the evolution of micro-fractures. Fibers are supposed to be ductile, and they are modeled by a variational plasticity model [41, 43], where plastic strains account for the inelastic processes experienced by the reinforcement. As in Aifantis's gradient plasticity theories [47, 48], the plastic energy is assumed to depend on the cumulated plastic strain, and it incorporates a nonlocal gradient term which allow to deal with stress-softening behaviours of plastic strains localization. In any material point, both the two phases coexist in proportion to their volume fraction, linked by elastic bonds, and thus fibres and matrix are indistinguishable in the resulting continuum body. A key modeling hypothesis is that all inelastic phenomena are included into damage and plastic properties of the two phases, and elastic bonds have just the role of transferring stresses between the two phases. The aim of this simplistic assumption is to separate the effects that each modelling ingredient has on the description of the failure process, keeping the analysis as simple as possible. It also allows for a straightforward calibration of the constitutive parameters.

Equilibrium equations and evolution laws for the internal state variables automatically descend from the energetic formulation, and, numerically, the evolution problem is formulated as an incremental energy minimization problem. Numerical solutions show the model ability to reproduce all the main features of the failure process of UHPFRC. The progressive formation of multiple micro-fractures within the brittle phase is reproduced, providing a more realistic description of the micro-cracking process than model [40], and the macro-crack growth occurring in the softening stage is described as a process of progressive plastic strain localization. In addition, the model correctly describes the dissipation mechanisms which, in experiments, are detected by performing unloading cycles, and which manifest in the form of stiffness degradation and residual strains.

Three different modeling levels of increasing complexity are considering. They correspond to a one-dimensional analytical scheme, a one-dimensional variational formulation and a three-dimensional variational model. The one-dimensional analytical theory highlights the fibres bridging mechanism across micro-cracks. It allows to correlate the spacing between adjacent micro-cracks to the value of the elastic coefficient of bonds between phases. Furthermore, the first-level model can be used as a fast design tool. At the second level, the one-dimensional variational formulation, preparatory to the three-dimensional extension, is used to determine the shapes of damage and plasticity energies, and to calibrate parameters therein. The damage energy is assumed to be linear to account for an initial elastic stage [25]. For the plastic energy, a convex-concave piecewise quadratic function is assigned in order to capture the two evolution stages of stress-hardening and stress-softening, characterized by plastic strain diffusion and localization. The one-dimensional scheme also allows to identify the three internal lengths incorporated into the model, which govern the entire failure process: the width of matrix micro-cracks, the size of the macro-fracture process zone, appearing in the non-local damage and plasticity energy contributions, respectively, and the minimum distance between adjacent micro-cracks, included in the elastic coefficient of the coupling bond energy. The three-dimensional variational model allows to simulate failure processes observed in real problems, capturing non-trivial crack patterning. The model is numerically implemented in a finite element code where the incremental minimum problem governing the failure evolution is solved through an iterative procedure which consists in sequences of constrained quadratic programming problems. Results of tensile and bending tests show the ability of the model in capturing the evolution of complex multiple cracks patterns, the accompanying development of plastic strains, and the final strain localization around a pre-existing micro-crack, which leads to the macro-fracture opening. The key role played by the three internal lengths on the entire failure process is pointed out, and, furthermore, special attention is focused on the dissipation mechanisms strictly closed to those observed in experiments.

The manuscript is organized as follows. In Sec. 2, the failure process observed in short-fiber reinforced composites is described, and the strategy to model it is presented, highlighting the basic modelling ideas. Sec. 3 introduces the preliminary analytical model, which allows for a first comprehension of the key features of the tensile failure observed in experiments. The variational model is introduced in Sec. 4. First, the theory is formulated, assigning the state variable and the energetic quantities, and deducing the governing equations, the dissipation inequalities and the incremental evolution problem. Then, the problem is reduced to the one dimensional setting, and the calibration issue is addressed. Different numerical examples are described in Sec. 5. Finally, conclusions and perspectives are drawn in Sec. 6.

Concerning notation, unless otherwise specified, a prime $\square'$ indicates either the derivative with respect to the spatial coordinate or the derivative with respect to the argument or the directional derivative of functionals; a superposed dot $\dot{\square}$ means right-derivative with respect to time.

2. Diffused fiber-reinforced composites

2.1. Failure process of UHPFRC in tensile experiments

In this section, we recall the main features of ductile failure of fiber-reinforced composites, as observed in tensile experiments. We concentrate on UHPFRC, which represent a specific class of composites made of brittle matrices strengthened with a significant amount of short fibers. The use of fibers (usually steel fibers) diffused into an ultra-high-performance concrete matrix remarkably enhances many mechanical properties, as strength and ductility, especially when tensile loads are applied [6, 49, 8, 50, 51, 52]. In Fig. 1, typical stress-strain curves resulting from direct tension tests on standard FRC and UHPFRC are compared. As it can be immediately noticed, the UHPFRC curve exhibits a stress-hardening branch, corresponding to progressive micro-cracking, which is totally absent in the responses of FRC or in standard plain concretes.

Three peculiar stages can be distinguished in the UHPFRC response curve of Fig. 1, which are described in the following.

i. Elastic stage. Initially the response is linearly elastic, and it terminates when the maximum tensile strength of the matrix is reached. At this instant, the first micro-crack forms within the matrix.

ii. Multi- and micro-cracking stage. By further loading, a sequence of cracks develops in the specimen. In this stage, the stress-strain curve has a sawtooth shape, where stress drops correspond to the opening of new cracks [50]. Since the upper envelop of the stress-strain curve is increasing, the overall response is stress-hardening[1]. Within each micro-fracture, bridging fibers transfer loads across the crack lips, preventing brittle failure and enhancing material ductility. This *bridging mechanism* [53] is accompanied by a process of plastic stress-hardening due to fibers plastic stretching and frictional debonding. The specimen can sustain increasing loadings because the strength of each cracked section, reinforced by fibers, is greater than the concrete matrix cracking strength.

Micro-cracks form more quickly in the first stage of the hardening process, and, as a result, stress drops are closer in the first part of the hardening branch of the response curve. As the process evolves, the frequency at which cracks open reduces. This multi-cracking stage terminates when the maximum strength of the reinforcement is achieved, and, at this point, the final softening stage starts.

At the end of the hardening stage, all cracks have experienced almost the same widening, as measured in [54] by using acoustic emission techniques, and they are almost equally spaced, as noticeable in pictures of Fig. 2. The ultimate cracks spacing, independent with respect to the bar length, is related to a characteristic internal length, which depends on the fibers geometrical and material properties and on their distribution within the matrix.

iii. Macro-crack opening stage. In this last stage, only a single pre-existing micro-crack continue to widen, turning into a macro-crack. Strains localize within the macro-crack, whereas the rest of the sample elastically unloads. The progressive breaking or pulling-out of bridging fibers leads to the sample failure. Macro-cracks are clearly visible in pictures of Fig. 2. Since the bar experiences a stress-softening behaviour, if it is sufficiently long, the response may be unstable (snap-back), with a deep stress drop and a brutal crack opening.

A sequence of unloadings and reloadings, as done in [8, 12], allows to estimate the evolution of damage and plasticity, by measuring the elastic modulus reduction and the permanent strain

[1] In many experimental works, stress drops are removed from the response curves, which present smooth branches.

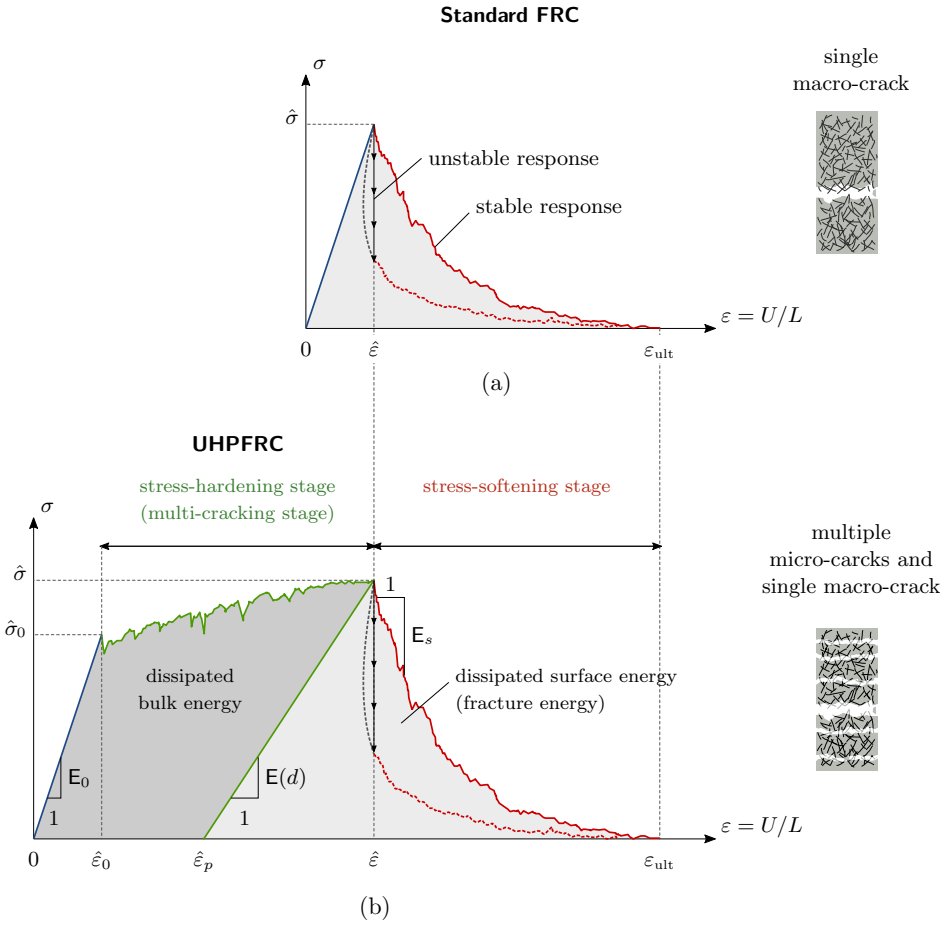

Figure 1: Responses of standard FRC (a) and UHPFRC (b) tensile specimens, with the corresponding failure crack pattern.

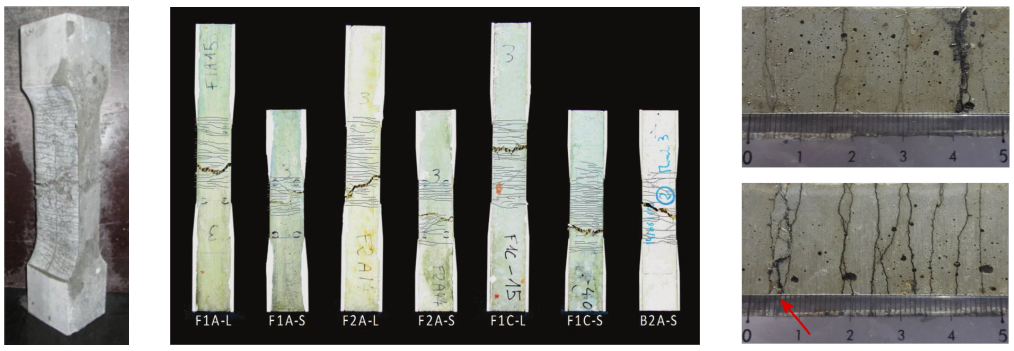

(a) (b) (c)

Figure 2: Crack pattern at failure of UHPFRC specimens subjected to direct tensile tests. In all situations, the cracks are always almost equally spaced, regardless their density, denoting the existence of a characteristic material length. Sub-figures (a), (b) and (c) are, respectively, taken from [6, 49, 51]

accumulation. Specifically, damage[2] mostly evolves at the beginning of the stress-hardening stage, thus being related to the evolution of micro-cracks. Differently, permanent inelastic strains, i.e. plastic strains, accumulate during the whole process, from the occurrence of the first crack to the specimen failure, growing about linearly. In the stress-hardening stage, plastic strains diffuse in the whole specimen, while, during the softening stage, they localize within the macro crack.

2.2. Composite modeling

Based on the above experimental evidences, we assume that a composite body Ω is a mixture of two solid phases, representing the matrix and the fiber reinforcement, respectively, bonded by elastic springs. Roman numbers I and II are used to label the two phases. The material of phase I is *brittle*, and a linear elastic-brittle constitutive law is assigned to it. Material of phase II is assumed to be elastic-plastic, and it is denominated *ductile* material. Volume fractions of the two phases are $v_{\rm I}$ and $v_{\rm II}$, with $v_{\rm I}+v_{\rm II}=1$. In the variational model proposed in Sec. 4, damage energy of phase I and plastic energy of phase II are endowed with non-local contributions which depend on two internal lengths, $\ell_{\rm I}$ and $\ell_{\rm II}$. The length $\ell_{\rm I}$ is related to the width of the fracture process zone of each micro-crack, whereas the length $\ell_{\rm II}$ represents the width of the plastic band that localizes in Ω when a macro-crack develops.

We assume that the reference configuration Ω is undeformed, stress-free, and without any pre-existing crack. For any point $x\in\Omega$, $\boldsymbol{u}_{\rm I}(x)$ and $\boldsymbol{u}_{\rm II}(x)$ are the displacements of the material points of phase I and II, respectively, and $\boldsymbol{\delta}(x)=\boldsymbol{u}_{\rm I}(x)-\boldsymbol{u}_{\rm II}(x)$ is their relative displacement.

Brittle and plastic phases are bonded by linear elastic springs. The forces that the two phases mutually exchange linearly depend on $\boldsymbol{\delta}$ through the elastic coefficient $\mathsf{E}_{\rm k}/\ell_{\rm k}^2$. The parameter $\ell_{\rm k}$ in the denominator is an internal length which controls the minimum spacing between adjacent micro-cracks, as shown in Sec. 3 through a simplified one-dimensional model. The stiffness modulus $\mathsf{E}_{\rm k}$ depends on the constitutive parameters of the two phases, and its explicit expression is deduced in Sec. 3. The model is based on the simplistic assumption that springs have just the task of elastically transferring stresses from one material phase to the other. All inelastic phenomena occurring at the interface level in real composites are included into the plastic properties of material II. This assumption is aimed at distinguishing the effects of the different model ingredients on the description of the composite failure process, and it allows to keep the analysis as simple as possible.

A geometrical sketch of the model is proposed in Fig. 3. Therein, the real composite and the model scheme are compared in case of sound and cracked configurations. The mixture proposed in the model is the superposition of two continua connected by springs, distinguished in the split view of Fig. 3.

3. 1D analytical model

We start discussing the mechanical response of a simple one-dimensional analytical model based on the modeling assumptions of Sec. 2.2, with the aim at reproducing the key features of the rich failure mechanism described in Sec. 2.1. Specifically, the domain Ω we consider consists of a bar of length L, made of the superposition of a brittle phase I and a ductile phase II, connected by elastic springs. A sketch of the problem geometry is proposed in Fig. 4a, where the split view is also reported.

For any $x\in(0,L)$, $u_{\rm I}(x)$ and $u_{\rm II}(x)$ are the axial displacements of points belonging to phase I and phase II, respectively. Since the aim is at reproducing failure in a tensile test, we assign

[2]Here damage refers to the elastic modulus reduction.

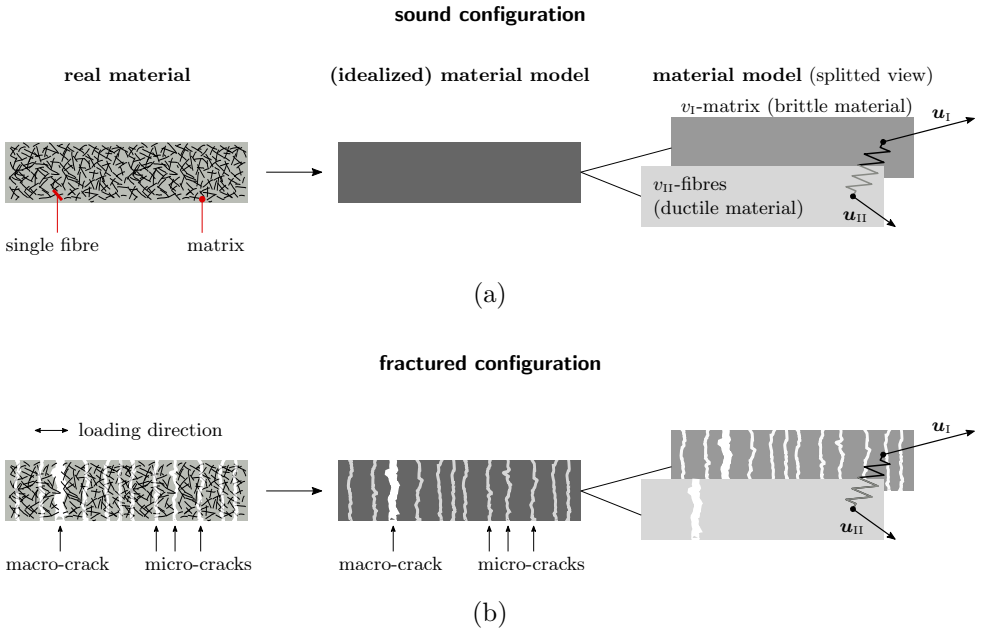

Figure 3: Real material and two-phases superposed continua represented for sound (a) and fractured (b) configurations.

the boundary conditions

$$u_{\mathrm{I}}(0) = u_{\mathrm{II}}(0) = 0 \qquad \text{and} \qquad u_{\mathrm{I}}(L) = u_{\mathrm{II}}(L) = \varepsilon(t)L \tag{3.1}$$

where $\varepsilon(t)$ is a given mean strain, function of time t.[3] We assume that $\varepsilon(0) = 0$, $\varepsilon(t) \geq 0$ and $\dot{\varepsilon}(t) \geq 0$, for any t. For sake of simplicity, only a positive not-decreasing ε is assigned, since this introductory model just intends to reproduce the cracking process observed in direct tension tests. The unloading behaviour is briefly addressed in Sec. 3.5.3. The infinitesimal strains of phase I and II, together with their relative displacement, are

$$\varepsilon_{\mathrm{I}} = u_{\mathrm{I}}', \qquad \varepsilon_{\mathrm{II}} = u_{\mathrm{II}}', \qquad \delta = u_{\mathrm{I}} - u_{\mathrm{II}} \tag{3.2}$$

and they are conjugated to the tensile stresses σ_{I} and σ_{II} and to the shear force τ. Relations between stresses and kinematic descriptors (3.2) are defined in the next section.

3.1. Constitutive assumptions

Phase I has a linear elastic-brittle behaviour. In the elastic stage, the tensile stress σ_{I} linearly depends on the stretching ε_{I} through the stiffness modulus E_{I}, and cracks open when a certain peak stress σ_{f} is reached. At fracture, the tensile stress nullifies since stiffness is totally lost. Accordingly, phase I obeys the following constitutive law

$$\sigma_{\mathrm{I}}(\varepsilon_{\mathrm{I}}) = \begin{cases} \mathsf{E}_{\mathrm{I}}\varepsilon_{\mathrm{I}}, & \text{if } \max_{\tau\in[0,t]}(\varepsilon_{\mathrm{I}}(\tau)) \leq \sigma_{\mathrm{f}}/\mathsf{E}_{\mathrm{I}} \\ 0, & \text{otherwise,} \end{cases} \tag{3.3}$$

whose graph is plotted in Fig. 5a.

[3] Here and in the following, the variable $t \in \mathbb{R}^+$, called *time* for convenience, is used to parameterize any deformation process.

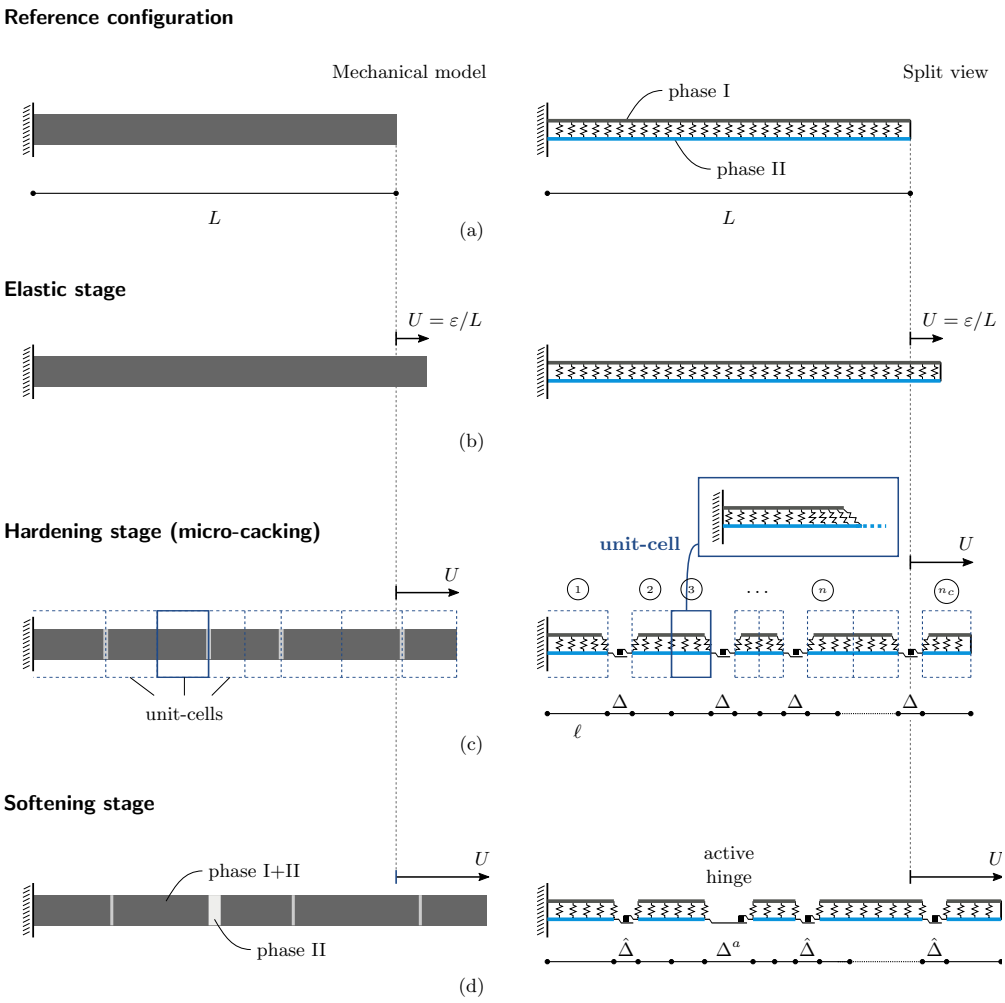

Figure 4: Geometrical scheme of the two-phases bar in the reference configuration (a), and in configurations associated to the three different evolution stages: the elastic stage (b), the hardening stage (c) and the softening stage (d).

Phase II is assumed to have a linear elastic behaviour, with stiffness modulus E_{II}, and plastic hinges can develop in those points where cracks are formed in phase I. In each hinge, the yield stress σ_{p} depends on the displacement jump

$$\Delta = u_{\mathrm{II}}^{+} - u_{\mathrm{II}}^{-}, \tag{3.4}$$

according to the bilinear hardening-softening law

$$\sigma_{\mathrm{p}}(\Delta) = \begin{cases} \mathsf{H}_{\mathrm{p}}\Delta + \bar{\sigma}_{\mathrm{p}}, & \text{if } 0 < \Delta \leq \hat{\Delta} \quad \text{(hardening)} \\ \hat{\sigma}_{\mathrm{p}} - \mathsf{S}_{\mathrm{p}}\left(\Delta - \hat{\Delta}\right), & \text{if } \hat{\Delta} < \Delta \leq \check{\Delta} \quad \text{(softening)} \\ 0, & \text{if } \check{\Delta} < \Delta \qquad \text{(hinge fracture)} \end{cases} \tag{3.5}$$

where

$$\mathsf{H}_{\mathrm{p}} = \frac{\hat{\sigma}_{\mathrm{p}} - \bar{\sigma}_{\mathrm{p}}}{\hat{\Delta}}, \qquad \text{and} \qquad \mathsf{S}_{\mathrm{p}} = \frac{\hat{\sigma}_{\mathrm{p}}}{\check{\Delta} - \hat{\Delta}}, \tag{3.6}$$

are the hardening and softening moduli. The choice of a bilinear yield stress function, with an hardening branch followed by a softening curve, is suggested by the response of UHPFRC

described in Sec. 2.1. After the elastic phase, the composite experiences a stress hardening phase in which plastic strains develop, as attested by the permanent strain registered at unloading, Fig. 1. Subsequently, the stress-softening stage takes place, where plastic strains localize in a single hinge and a macro-crack opens. The parameters to be assigned in (3.5) are the activation stress $\bar{\sigma}_{\rm p}$, the point $(\hat{\Delta}, \hat{\sigma}_{\rm p})$ of maximum stress, and the displacement jump $\check{\Delta}$ at complete failure. A graph of the yield stress is drawn in Fig. 5b. In each hinge, displacement jump Δ and stress $\sigma_{\rm II}$ evolve according to the set of Kuhn-Tucker conditions

$$\sigma_{\rm II} \le \sigma_{\rm p}(\Delta) \quad \dot{\Delta} \ge 0 \quad (\sigma_{\rm p}(\Delta) - \sigma_{\rm II})\, \dot{\Delta} = 0, \tag{3.7}$$

which state that Δ never decreases, and that it can increases only if $\sigma_{\rm II}$ equals $\sigma_{\rm p}$.

Lastly, we assume that springs connecting phase I and phase II are linear elastic. Accordingly, relation between shear stress τ and relative displacement δ is

$$\tau = \frac{\mathsf{E}_{\rm k}}{\ell_{\rm k}^2}\delta. \tag{3.8}$$

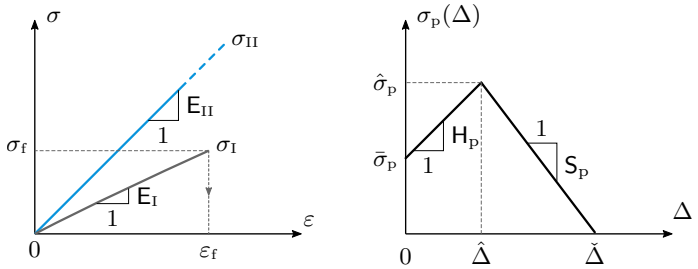

(a) (b)

Figure 5: Constitutive laws. (a) Fracture law of phase I, (b) plastic law of phase II.

3.2. Equilibrium configurations

Increasing ε, we expect an initial elastic stretching, Fig. 4b, followed by a stress-hardening phase, in which a sequence of cracks forms in phase I, and plastic hinges develop in phase II, Fig. 4c. Finally, when one hinge enters the softening regime, its plastic displacement increases, leading the bar to failure, Fig. 4d. In the fractured configurations of Figs. 4c-d, adjacent cracks are separated by portions of sound bar. Each portion is divided into two symmetric parts of equal length that are called *unit-cells*. In case cracks cannot form at the bar endpoints, $2n$ unit-cells correspond to n cracks. Within each unit-cell, stresses in the two phases are

$$\sigma_{\rm I}(x) = \mathsf{E}_{\rm I}\varepsilon_{\rm I}(x), \quad \sigma_{\rm II}(x) = \mathsf{E}_{\rm II}\varepsilon_{\rm II}(x), \tag{3.9}$$

and the global stress is

$$\sigma(x) = v_{\rm I}\sigma_{\rm I}(x) + v_{\rm II}\sigma_{\rm II}(x). \tag{3.10}$$

An enlargement of the generic i-th unit-cell of length ℓ_i is sketched in Fig. 6a. In the following, index i is omitted for brevity.

Equilibrium equations, easily deduced from the scheme drawn in Fig. 6b, are

$$v_{\rm I}\sigma_{\rm I}' - \tau = 0, \qquad v_{\rm II}\sigma_{\rm II}' + \tau = 0. \tag{3.11}$$

We notice that, summing up the two equations, we obtain

$$v_{\rm I}\sigma_{\rm I}' + v_{\rm II}\sigma_{\rm II}' = (v_{\rm I}\sigma_{\rm I} + v_{\rm II}\sigma_{\rm II})' = \sigma' = 0, \tag{3.12}$$

which says that the total stress σ is constant trough the bar. If we substitute (3.8) in (3.11) and differentiate, equilibrium equations rewrite as follows

$$v_{\mathrm{I}}\mathsf{E}_{\mathrm{I}}\varepsilon_{\mathrm{I}}'' = \frac{\mathsf{E}_{\mathrm{k}}}{\ell_{\mathrm{k}}^2}(\varepsilon_{\mathrm{I}} - \varepsilon_{\mathrm{II}}), \qquad v_{\mathrm{II}}\mathsf{E}_{\mathrm{II}}\varepsilon_{\mathrm{II}}'' = -\frac{\mathsf{E}_{\mathrm{k}}}{\ell_{\mathrm{k}}^2}(\varepsilon_{\mathrm{I}} - \varepsilon_{\mathrm{II}}). \tag{3.13}$$

In order to solve these set of ordinary differential equations, pairs of boundary conditions for ε_{I} and $\varepsilon_{\mathrm{II}}$ are needed. Referring to the local reference system plotted in Fig. 6a, we assign the conditions

$$\varepsilon_{\mathrm{I}}'(0) = 0, \quad \varepsilon_{\mathrm{II}}'(0) = 0, \quad \varepsilon_{\mathrm{I}}(\ell) = 0, \quad \varepsilon_{\mathrm{II}}(\ell) = \tilde{\varepsilon}. \tag{3.14}$$

The first two conditions result from the symmetry of strains with respect to the midpoint of each sound portion between consecutive cracks. The third condition is due to the fact that phase I is fractured at $x = \ell$. The fourth condition assumes that the strain adjacent to a possible plastic hinge is equal to a positive strain $\tilde{\varepsilon}$, which will be determined later on from the kinematic compatibility equation.

Solution of problem (3.13)-(3.14) is

$$\varepsilon_{\mathrm{I}}(x) = \frac{\tilde{\varepsilon}}{1+\beta}\left(1 - \frac{\cosh(\kappa x)}{\cosh(\kappa \ell)}\right), \quad \varepsilon_{\mathrm{II}}(x) = \frac{\tilde{\varepsilon}}{1+\beta}\left(1 + \beta\frac{\cosh(\kappa x)}{\cosh(\kappa \ell)}\right) \tag{3.15}$$

with

$$\beta = \frac{v_{\mathrm{I}}\mathsf{E}_{\mathrm{I}}}{v_{\mathrm{II}}\mathsf{E}_{\mathrm{II}}}, \qquad \kappa = \frac{1}{\ell_{\mathrm{k}}}\sqrt{\mathsf{E}_{\mathrm{k}}\left(\frac{1}{v_{\mathrm{I}}\mathsf{E}_{\mathrm{I}}} + \frac{1}{v_{\mathrm{II}}\mathsf{E}_{\mathrm{II}}}\right)} \tag{3.16}$$

Since the strain fields ε_{I} and $\varepsilon_{\mathrm{II}}$ of solution (3.15) are monotone concave and convex, respectively (see Fig. 7), we can easily evaluate the maximum stresses σ_{I} and σ_{II}. By using (3.9) and (3.15), we get

$$\begin{aligned} &\max_x \mathsf{E}_{\mathrm{I}}\,\varepsilon_{\mathrm{I}}(x) = \mathsf{E}_{\mathrm{I}}\,\varepsilon_{\mathrm{I}}(0) = d(\ell)\tilde{\varepsilon} =: \sigma_{\mathrm{I}}^{\max}(\ell, \tilde{\varepsilon}) \\ &\max_x \mathsf{E}_{\mathrm{II}}\,\varepsilon_{\mathrm{II}}(x) = \mathsf{E}_{\mathrm{II}}\,\varepsilon_{\mathrm{II}}(\ell) = \mathsf{E}_{\mathrm{II}}\,\tilde{\varepsilon} =: \sigma_{\mathrm{II}}^{\max}(\tilde{\varepsilon}) \end{aligned} \tag{3.17}$$

with

$$d(\ell) = \frac{\mathsf{E}_{\mathrm{I}}}{1+\beta}\left(1 - \frac{1}{\cosh(\kappa \ell)}\right). \tag{3.18}$$

We notice that $\sigma_{\mathrm{II}}^{\max}$ is the stress applied to the plastic hinge. Being $\sigma_{\mathrm{I}}(l) = 0$ and $\sigma_{\mathrm{II}}(l) = \sigma_{\mathrm{II}}^{\max}$, the global stress (3.10) is

$$\sigma = v_{\mathrm{II}}\sigma_{\mathrm{II}}^{\max} = v_{\mathrm{II}}\mathsf{E}_{\mathrm{II}}\,\tilde{\varepsilon}. \tag{3.19}$$

Since σ is constant along the bar, $\tilde{\varepsilon}$ is the strain of all points of phase II which are adjacent to plastic hinges, and, consequently, all hinges have the same stress, equal to $\sigma_{\mathrm{II}}^{\max}$.

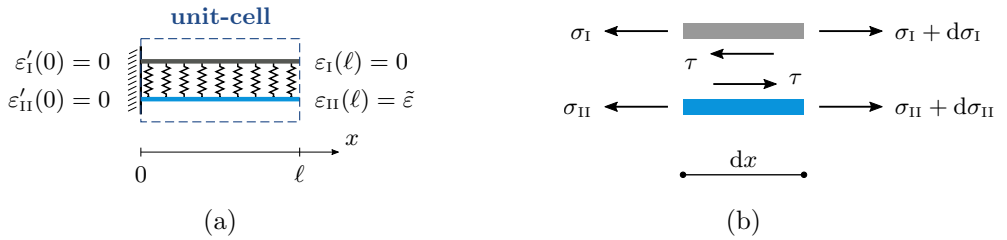

Figure 6: (a) Unit-cell problem with corresponding boundary conditions, (b) forces in an infinitesimal portion of the bar.

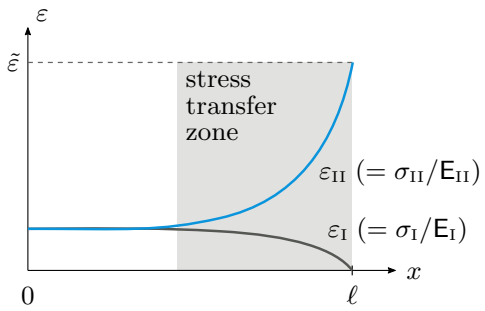

Figure 7: Strain profiles and stress transfer zone within a unit cell.

3.3. Micro-cracks spacing

In each bar portion of length $2\ell_i$ between adjacent cracks, the maximum stress $\sigma_{\mathrm{I}}^{\max}$ in phase I is attained at the midpoint, and its value is proportional to the half-length ℓ_i, namely

$$\sigma_{\mathrm{I}}^{\max}(\ell_1, \tilde{\varepsilon}) > \sigma_{\mathrm{I}}^{\max}(\ell_2, \tilde{\varepsilon}) \quad \text{if} \quad \ell_1 > \ell_2. \tag{3.20}$$

Consequently, within each unit-cell, a new crack forms at the sound endpoint $x = 0$, Fig. 6a, when the peak stress σ_{f} is reached, according to the stress criterion (3.3). Condition for crack opening writes

$$\sigma_{\mathrm{I}}^{\max}(\ell, \tilde{\varepsilon}) = \sigma_{\mathrm{f}}, \tag{3.21}$$

from which, using $(3.17)_1$, the maximum strain $\tilde{\varepsilon}$ is

$$\tilde{\varepsilon}_{\mathrm{f}} = \sigma_{\mathrm{f}}/d(\ell). \tag{3.22}$$

During the micro-cracking process, each new crack opens in the longest unit-cell, where the largest $\sigma_{\mathrm{I}}^{\max}$ is attained.

Let us suppose that, within a unit cell, stresses $\sigma_{\mathrm{I}}^{\max}$ and $\sigma_{\mathrm{II}}^{\max}$ assume the values

$$\sigma_{\mathrm{I}}^{\max} = d(\ell)\tilde{\varepsilon} = \sigma_{\mathrm{f}}, \qquad \sigma_{\mathrm{II}}^{\max} = \mathsf{E}_{\mathrm{II}}\tilde{\varepsilon} = \hat{\sigma}_{\mathrm{p}}. \tag{3.23}$$

The first equation represents the condition for which a new fracture opens in material I, and the second equation represents the condition for which the peak stress in material II is achieved. By further increasing the strain ε, two different evolutions are possible: *i.* a new crack forms, which produces a stress drop; the plastic hinge reenters in the stress-hardening phase, and the micro-cracking process goes on; *ii.* the plastic hinge starts the softening phase, and its plastic displacement increases; the global stress reduces in the whole bar, and no further cracks form.

If we solve equations (3.23) with respect to ℓ and $\tilde{\varepsilon}$, we obtain the critical length

$$\ell = \hat{\ell} := \ell_{\mathrm{k}} \frac{\operatorname{arc\,sech}\left(1 - (1+\beta)\dfrac{\mathsf{E}_{\mathrm{II}}\sigma_{\mathrm{f}}}{\mathsf{E}_{\mathrm{I}}\hat{\sigma}_{\mathrm{p}}}\right)}{\sqrt{\mathsf{E}_{\mathrm{k}}\left(\dfrac{1}{v_{\mathrm{I}}\mathsf{E}_{\mathrm{I}}} + \dfrac{1}{v_{\mathrm{II}}\mathsf{E}_{\mathrm{II}}}\right)}}. \tag{3.24}$$

If the half-spacing length is slightly larger than $\hat{\ell}$, evolution *i.* is favored and a new crack forms. The resulting half-spacing becomes $\hat{\ell}/2$, which represents lower estimate of the semi-distance between adjacent cracks. On the contrary, if the half-spacing length is a bit smaller than $\hat{\ell}$, evolution *ii.* takes place.

Eq. (3.24) allows us to calibrate the internal length $\ell_{\rm k}$ and the modulus $\mathsf{E}_{\rm k}$ as follows. We assign to $\ell_{\rm k}$ the value of the smallest micro-crack spacing observed in tensile experiments at the end of the stress-hardening stage. Since the half-spacing lower bound is $\hat{\ell}/2$, we set $\hat{\ell} = \ell_{\rm k}$ in (3.24), from which we obtain

$$\mathsf{E}_{\rm k} = \frac{\left(\operatorname{arc\,sech}\left(1-(1+\beta)\dfrac{\mathsf{E}_{\rm II}\sigma_{\rm f}}{\mathsf{E}_{\rm I}\hat{\sigma}_{\rm p}}\right)\right)^2}{\dfrac{1}{v_{\rm I}\mathsf{E}_{\rm I}}+\dfrac{1}{v_{\rm II}\mathsf{E}_{\rm II}}}, \tag{3.25}$$

which allows to set the value of $\mathsf{E}_{\rm k}$ as function of the phases volume ratios $v_{\rm I}$ and $v_{\rm II}$, Young's moduli $\mathsf{E}_{\rm I}$ and $\mathsf{E}_{\rm II}$, and peak stresses $\sigma_{\rm f}$ and $\hat{\sigma}_{\rm p}$ that phases can achieve.

3.4. Kinematical compatibility

To determine the unknown strain $\tilde{\varepsilon}$, we require the solution to be kinematical compatible. The compatibility equation reads

$$\varepsilon L = \sum_{h=1}^{2n}\int_0^{\ell_h}\varepsilon_{\rm II}(x)\,{\rm d}x + \sum_{i=1}^{n}\Delta_i, \tag{3.26}$$

which states that the bar elongation (term on the left-hand side) is given by two contributions: the elastic stretching of the unit-cells (first summation on the right-hand side), and the elongations Δ_i of the plastic hinges (second summation on the right-hand side). Using $(3.15)_2$, the integral in the first summation reads

$$\int_0^{\ell_h}\varepsilon_{\rm II}(x)\,{\rm d}x = f(\ell_h)\tilde{\varepsilon}, \qquad \text{with} \quad f(\ell) = \frac{\kappa\ell+\beta\tanh(\kappa\ell)}{(1+\beta)\kappa} \tag{3.27}$$

and the corresponding summation rewrites

$$\sum_{h=1}^{2n}\int_0^{\ell_h}\varepsilon_{\rm II}(x)\,{\rm d}x = S(\mathcal{L}_n)\tilde{\varepsilon} \tag{3.28}$$

with

$$S(\mathcal{L}_n) = \sum_{h=1}^{2n} f(\ell_h) \quad \text{and} \quad \mathcal{L}_n = \{\ell_h, h=1,\dots,2n\}\,. \tag{3.29}$$

We suppose that the n plastic hinges, corresponding to the n micro-fractures, are in stress-hardening regime, i.e., $\Delta_i \le \hat{\Delta}$, for any $i = 1, ..., n$, and that j hinges are active and $(n-j)$ are inactive. In an active hinge, stress equals the yield stress $\sigma_{\rm II}^{\max} = \sigma_{\rm p}(\Delta_i)$, and the plastic displacement Δ_i evolves ($\dot{\Delta}_i > 0$). On the contrary, in an inactive hinge, $\sigma_{\rm II}^{\max} < \sigma_{\rm p}(\Delta_i)$, and Δ_i stays fixed ($\dot{\Delta}_i = 0$).

In case of an active hinge, from equation $\sigma_{\rm II}^{\max} = \sigma_{\rm p}(\Delta_i)$, by using (3.5) and $(3.17)_2$, we obtain

$$\Delta_i := \Delta^a = \frac{1}{\mathsf{H}_{\rm p}}\left(\mathsf{E}_{\rm II}\tilde{\varepsilon} - \bar{\sigma}_{\rm p}\right), \tag{3.30}$$

which states that all active hinges have the same plastic displacement Δ^a, where a stands for *active*. We assume that all inactive hinges have the same plastic displacement jump, Δ^f, where f stands for *fixed*. Since $\sigma_{\rm II}^{\max} = \sigma_{\rm p}(\Delta^a) < \sigma_{\rm p}(\Delta^f)$ and $\sigma_{\rm p}$ is increasing with Δ in the considered case of stress-hardening, then $\Delta^a < \Delta^f$. Equation (3.26) rewrites

$$\varepsilon L = S(\mathcal{L}_n)\tilde{\varepsilon} + \frac{j}{\mathsf{H}_\mathrm{p}}\left(\mathsf{E}_\mathrm{II}\tilde{\varepsilon} - \bar{\sigma}_\mathrm{p}\right) + (n-j)\Delta^f, \tag{3.31}$$

from which

$$\tilde{\varepsilon} = \tilde{\varepsilon}(\varepsilon, n, j, \mathcal{L}_n, \Delta^f) = c_1(j, \mathcal{L}_n)\varepsilon + c_2(n, j, \mathcal{L}_n, \Delta^f), \tag{3.32}$$

with

$$\begin{aligned} c_1(j, \mathcal{L}_n) &= \frac{L}{S(\mathcal{L}_n) + j\mathsf{E}_\mathrm{II}/\mathsf{H}_\mathrm{p}} \\ c_2(n, j, \mathcal{L}_n, \Delta^f) &= \frac{c_1(n, j, \mathcal{L}_n)}{L}\left(j\frac{\bar{\sigma}_\mathrm{p}}{\mathsf{H}_\mathrm{p}} - (n-j)\Delta^f\right). \end{aligned} \tag{3.33}$$

For future developments, it is useful to invert (3.32) and to express ε in terms of $\tilde{\varepsilon}$

$$\varepsilon = \frac{1}{c_1(j, \mathcal{L}_n)}\left(\tilde{\varepsilon} - c_2(n, j, \mathcal{L}_n, \Delta^f)\right). \tag{3.34}$$

3.5. Evolution

In the forthcoming sections, we analyze the three different stages, namely the elastic, the hardening and the softening stages, which are experienced by the bar in a tensile test.

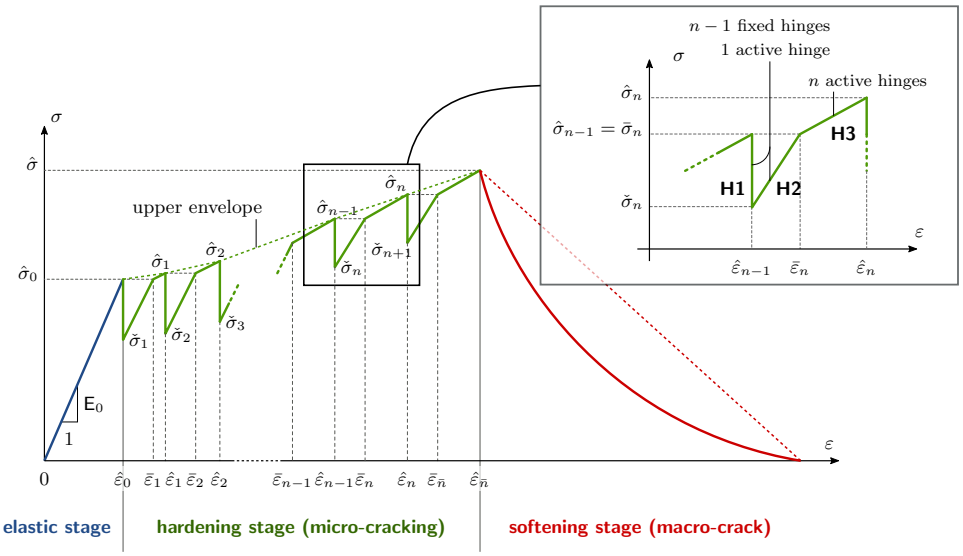

Figure 8: Schematic graph of the $\sigma - \varepsilon$ curve, where the different response stages are highlighted. The green and red dashed lines represent, respectively, the envelop of all local stress peaks and a linear approximation of the softening stage.

3.5.1. Elastic stage

Initially, the bar undergoes a linear elastic stretching, according to the law

$$\sigma = (v_\mathrm{I}\mathsf{E}_\mathrm{I} + v_\mathrm{II}\mathsf{E}_\mathrm{II})\,\varepsilon. \tag{3.35}$$

Strains are uniform along the bar and equal to ε in the two materials, and since $\delta = 0$, the connecting springs are unloaded, with $\tau = 0$.

As soon as the stress in phase I reaches the value $\sigma_{\rm f}$, a fracture opens in the brittle phase. Global strain and stress at the end of the elastic stage are

$$\hat{\varepsilon}_0 = \sigma_{\rm f}/\mathsf{E}_{\rm I}, \quad \text{and} \quad \hat{\sigma}_0 = \frac{v_{\rm I}\mathsf{E}_{\rm I} + v_{\rm II}\mathsf{E}_{\rm II}}{\mathsf{E}_{\rm I}}\sigma_{\rm f}, \tag{3.36}$$

(see Fig. 8).

After the occurrence of the first fracture, the stress is no more homogeneous through the bar. Indeed, at fracture, $\sigma_{\rm I}$ drops to zero, and $\sigma_{\rm II}$ jumps up to a sufficiently high value for plastic hinge activation. By using $(3.17)_2$ and (3.32), the stress at the hinge is

$$\sigma_{\rm II} = \sigma_{\rm II}^{\max} = \mathsf{E}_{\rm II}\,\tilde{\varepsilon}(\hat{\varepsilon}_0, 1, 1, \mathcal{L}_1, 0). \tag{3.37}$$

Arguments of function $\tilde{\varepsilon}$ account for a single active hinge between two unit-cells. The plastic hinge activates after the crack occurrence only if the activation stress $\bar{\sigma}_{\rm p}$ in (3.5) satisfies the inequalities

$$\bar{\sigma}_{\rm p} \geq (\mathsf{E}_{\rm II}/\mathsf{E}_{\rm I})\sigma_{\rm f}, \qquad \bar{\sigma}_{\rm p} \leq \sigma_{\rm II}^{\max}. \tag{3.38}$$

The first inequality avoids hinge activation before crack opening, and the second one guaranties hinge activation after breaking. When the first crack and hinge form, the global stress (3.19) drops down to the value

$$\check{\sigma}_1 = v_{\rm II}\mathsf{E}_{\rm II}\,\tilde{\varepsilon}(\hat{\varepsilon}_0, 1, 1, \mathcal{L}_1, 0), \tag{3.39}$$

as shown in Fig. 8.

3.5.2. Micro-cracking stage

After the occurrence of the first fracture, the process of progressive cracks opening takes place in a stress-hardening regime. The resulting stress-strain curve has a sawtooth shape, where stress drops correspond to crack openings. We suppose that one crack forms at a time, and we do not consider simultaneous opening of multiple cracks. The micro-cracking response is obtained by recursively repeating three stages sketched in the enlargement of Fig. 8 and highlighted by labels **H1**, **H2** and **H3**, which define one tooth of the stress-hardening curve of Fig. 8. Notice that each branch is linear since linear constitutive laws have been assumed.

We analyze each stage, supposing that the bar has $(n-1)$ cracks and $(n-1)$ hinges, and that the initial point $(\hat{\varepsilon}_{n-1}, \hat{\sigma}_{n-1})$ is known. It is also known the plastic elongation Δ_{n-1} of the $(n-1)$ hinges. Combining $(3.17)_2$ and (3.19), stress and strain at the $(n-1)$ hinges are

$$\sigma_{\rm II}^{\max} = \frac{\hat{\sigma}_{n-1}}{v_{\rm II}}, \qquad \tilde{\varepsilon} = \frac{\hat{\sigma}_{n-1}}{v_{\rm II}\mathsf{E}_{\rm II}}. \tag{3.40}$$

Stage H1, from $(\hat{\varepsilon}_{n-1}, \hat{\sigma}_{n-1})$ to $(\hat{\varepsilon}_{n-1}, \check{\sigma}_n)$. The new n-th crack opens and the corresponding plastic n-th hinge forms. The stress drops to the value

$$\check{\sigma}_n = v_{\rm II}\mathsf{E}_{\rm II}\,\tilde{\varepsilon}(\hat{\varepsilon}_{n-1}, n, 1, \mathcal{L}_n, \Delta_{n-1}), \tag{3.41}$$

which is obtained by (3.19) and (3.32). Arguments of $\tilde{\varepsilon}$ account for $(n-1)$ inactive pre-existing hinges, with plastic elongation Δ_{n-1}, and one active new-formed hinge. At crack opening, the plastic displacement of the active hinge is given by (3.30), with $\tilde{\varepsilon} = \tilde{\varepsilon}(\hat{\varepsilon}_{n-1}, n, 1, \mathcal{L}_n, \Delta_{n-1})$.

Stage H2, from $(\hat{\varepsilon}_{n-1}, \check{\sigma}_n)$ to $(\bar{\varepsilon}_n, \bar{\sigma}_n)$. By increasing ε after the stress drop, unit-cells elastically reload. The plastic elongation of the new appeared plastic hinge increases, while the $(n-1)$ inactive hinges stay fixed. This stage terminates when the elongation Δ^a of the active hinge reaches the elongation Δ_{n-1} of the inactive hinges. At this point, stress $\sigma_{\rm II}^{\max}$ and strain $\tilde{\varepsilon}$ of the

active hinge equal the values (3.40) of the inactive hinges. From now on, all hinges are active. At the end of phase **H2**, the global stress is

$$\bar{\sigma}_n = \hat{\sigma}_{n-1}, \tag{3.42}$$

and the corresponding global strain $\bar{\varepsilon}_n$, determined from (3.34) and $(3.40)_2$, is

$$\bar{\varepsilon}_n = \frac{1}{c_1(0,\mathcal{L}_n)}\left(\frac{\hat{\sigma}_{n-1}}{v_{\rm II}\mathsf{E}_{\rm II}} - c_2(n,0,\mathcal{L}_n,\Delta_{n-1})\right). \tag{3.43}$$

Parameters of c_1 and c_2 account for n hinges with plastic displacement Δ_{n-1}.

Stage H3, from $(\bar{\varepsilon}_n,\bar{\sigma}_n)$ to $(\hat{\varepsilon}_n,\hat{\sigma}_n)$. In this phase, plastic displacements develop in all the n hinges, and unit-cells elastically stretch. The global stress-strain response is still linear, but with a smaller slope than in stage **H2**, since all plastic hinges are active now. This stage terminates when the stress $\sigma_{\rm I}$ attains the peak value $\sigma_{\rm f}$ in one unit-cell, and strain $\tilde{\varepsilon}$ equals the peak value $\tilde{\varepsilon}_{\rm f}$ given by (3.22). Values of $\hat{\varepsilon}_n$ and $\hat{\sigma}_n$ are determined from (3.34) and (3.19), respectively, with $\tilde{\varepsilon} = \tilde{\varepsilon}_{\rm f}$. They are

$$\hat{\varepsilon}_n = \frac{1}{c_1(n,\mathcal{L}_n)}\left(\tilde{\varepsilon}_{\rm f} - c_2(n,n,\mathcal{L}_n,0)\right), \qquad \hat{\sigma}_n = v_{\rm II}\mathsf{E}_{\rm II}\tilde{\varepsilon}_{\rm f}, \tag{3.44}$$

where n active hinges are considered to set the variables of c_1 and c_2. The final plastic displacement of hinges is

$$\Delta_n = \frac{1}{\mathsf{H}_{\rm p}}\left(\mathsf{E}_{\rm II}\tilde{\varepsilon}_{\rm f} - \bar{\sigma}_{\rm p}\right). \tag{3.45}$$

3.5.3. Macro-crack opening stage

The hardening stage finishes when the peak stress $\hat{\sigma}_{\rm p}$ is reached in the plastic hinges. At this instant, the number of fractures is

$$\bar{n} : \underset{n\,:\,\hat{\sigma}_n \geq \hat{\sigma}_{\rm p}}{\arg\min}\ \hat{\sigma}_n, \tag{3.46}$$

and, by using (3.19), the global stress is

$$\hat{\sigma}_{\bar{n}} = v_{\rm II}\hat{\sigma}_{\rm p}. \tag{3.47}$$

The corresponding global strain, determined by equation (3.34) with $\tilde{\varepsilon} = \hat{\sigma}_{\rm p}/\mathsf{E}_{\rm II}$, is

$$\hat{\varepsilon}_{\bar{n}} = \frac{1}{c_1(\bar{n},\mathcal{L}_{\bar{n}})}\left(\frac{\hat{\sigma}_{\rm p}}{\mathsf{E}_{\rm II}} - c_2(\bar{n},\bar{n},\mathcal{L}_{\bar{n}},0)\right), \tag{3.48}$$

where $\bar{n}$ active hinges are taken into account, whose plastic displacement is $\hat{\Delta}$, introduced in (3.5). From this point on, we suppose that $(\hat{n}-1)$ hinges remain inactive, and only one hinge evolves. According to the constitutive law (3.5), the plastic displacement $\Delta^a \in (\hat{\Delta},\check{\Delta})$ of the considered active hinge is obtained by inverting the relation $\sigma_{\rm II}^{\max} = \sigma_{\rm p}(\Delta^a)$, and its expression is

$$\Delta^a = \frac{1}{\mathsf{S}_{\rm p}}\left(\hat{\sigma}_{\rm p} - \mathsf{E}_{\rm II}\tilde{\varepsilon}\right) + \hat{\Delta}. \tag{3.49}$$

In this case of one active hinge in stress-softening regime, and $\bar{n}-1$ inactive hinges with displacement $\hat{\Delta}$, the compatibility equation (3.26) writes

$$\varepsilon L = S(\mathcal{L}_{\bar{n}})\tilde{\varepsilon} + \frac{1}{\mathsf{S}_{\rm p}}\left(\hat{\sigma}_{\rm p} - \mathsf{E}_{\rm II}\tilde{\varepsilon}\right) + \bar{n}\hat{\Delta}, \tag{3.50}$$

from which

$$\tilde{\varepsilon} = d_1(\mathcal{L}_{\bar{n}})\varepsilon + d_2(\bar{n}, \mathcal{L}_{\bar{n}}), \tag{3.51}$$

with

$$d_1(\mathcal{L}_{\bar{n}}) = \frac{L}{S(\mathcal{L}_{\bar{n}}) - \mathsf{E}_{\mathrm{II}}/\mathsf{S}_{\mathrm{p}}}, \quad d_2(\bar{n}, \mathcal{L}_{\bar{n}}) = -\frac{d_1(\mathcal{L}_{\bar{n}})}{L}\left(\frac{\hat{\sigma}_{\mathrm{p}}}{\mathsf{S}_{\mathrm{p}}} + \bar{n}\hat{\Delta}\right). \tag{3.52}$$

By combining (3.51) and (3.19), the stress-strain law for the stress-softening stage reads

$$\sigma = v_{\mathrm{II}}\mathsf{E}_{\mathrm{II}}\left(d_1(\mathcal{L}_{\bar{n}})\varepsilon + d_2(\bar{n}, \mathcal{L}_{\bar{n}})\right). \tag{3.53}$$

The stress σ decreases for increasing ε, and it nullifies when the ultimate strain

$$\varepsilon_{\mathrm{ult}} = -\frac{d_2(\bar{n}, \mathcal{L}_{\bar{n}})}{d_1(\mathcal{L}_{\bar{n}})} = \frac{1}{L}\left(\frac{\hat{\sigma}_{\mathrm{p}}}{\mathsf{S}_{\mathrm{p}}} + \bar{n}\hat{\Delta}\right) \tag{3.54}$$

is reached. Necessary condition for the stress-softening evolution is that $d_1 \leq 0$, which, from $(3.52)_1$, corresponds to

$$\mathsf{E}_{\mathrm{II}}/\mathsf{S}_{\mathrm{p}} \geq S(\mathcal{L}_{\bar{n}}). \tag{3.55}$$

If this inequality is not satisfied, the bar undergoes brutal failure (snap-back).

Remark. The above analysis does not change if we consider more complex yield stress functions than (3.5). Only few equations require slight modifications. Let us assume the generic yield stress law

$$\sigma_{\mathrm{p}}(\Delta) = \begin{cases} \sigma_{\mathrm{p}}^h(\Delta), & \text{if } 0 \leq \Delta < \hat{\Delta} \\ \sigma_{\mathrm{p}}^s(\Delta), & \text{if } \Delta \geq \hat{\Delta} \end{cases} \tag{3.56}$$

where $\sigma_{\mathrm{p}}^h(\Delta)$ and $\sigma_{\mathrm{p}}^s(\Delta)$ are continuous functions, accounting for hardening and softening responses, and satisfying the properties:

$$\begin{aligned} &\sigma_{\mathrm{p}}^h(0) = \bar{\sigma}_{\mathrm{p}}, \quad \sigma_{\mathrm{p}}^h(\hat{\Delta}) = \sigma_{\mathrm{p}}^s(\hat{\Delta}) = \hat{\sigma}_{\mathrm{p}}, \quad \frac{\mathrm{d}\sigma_{\mathrm{p}}^h}{\mathrm{d}\Delta}(\hat{\Delta}) = \frac{\mathrm{d}\sigma_{\mathrm{p}}^s}{\mathrm{d}\Delta}(\hat{\Delta}) = 0, \quad \sigma_{\mathrm{p}}^s(\Delta) \geq 0, \\ &\begin{cases} \dfrac{\mathrm{d}\sigma_{\mathrm{p}}^h}{\mathrm{d}\Delta}(\Delta) > 0, & \text{if } 0 \leq \Delta < \hat{\Delta} \\ \dfrac{\mathrm{d}\sigma_{\mathrm{p}}^s}{\mathrm{d}\Delta}(\Delta) < 0, & \text{if } \Delta > \hat{\Delta} \end{cases}. \end{aligned} \tag{3.57}$$

Each function is invertible, because it is continuous and monotonic. As a result of the assumption (3.56), equations (3.30) and (3.49) modify as follows

$$\Delta^a = (\sigma_{\mathrm{p}}^h)^{-1}(\mathsf{E}_{\mathrm{II}}\tilde{\varepsilon}), \quad \Delta^a = (\sigma_{\mathrm{p}}^s)^{-1}(\mathsf{E}_{\mathrm{II}}\tilde{\varepsilon}), \tag{3.58}$$

and the kinematic compatibility conditions (3.31) and (3.50) rewrite, respectively, in the form

$$\begin{aligned} \varepsilon L &= S(\mathcal{L}_n)\tilde{\varepsilon} + j\,(\sigma_{\mathrm{p}}^h)^{-1}(\mathsf{E}_{\mathrm{II}}\tilde{\varepsilon}) + (n-j)\Delta^f, \\ \varepsilon L &= S(\mathcal{L}_{\bar{n}})\tilde{\varepsilon} + (\sigma_{\mathrm{p}}^s)^{-1}(\mathsf{E}_{\mathrm{II}}\tilde{\varepsilon}) + (\bar{n}-1)\hat{\Delta}, \end{aligned} \tag{3.59}$$

which are solved with respect to $\tilde{\varepsilon}$.

3.6. Global response

In the previous section, all key steps for deducing the global σ-ε curve of a tensile test have been derived, with the underlying assumption that multiple cracks are not allowed to occur simultaneously. Summing up, each branch of the curve is linear and determined by means of the following relations:

- elastic stage:
  - $(\hat{\varepsilon}_0,\, \hat{\sigma}_0) \mapsto$ (3.36);
- hardening stage:
  - $(\hat{\varepsilon}_{n-1}, \check{\sigma}_n) \mapsto$ (3.41);
  - $(\bar{\varepsilon}_n, \bar{\sigma}_n) \mapsto$ (3.42)-(3.43);
  - $(\hat{\varepsilon}_n, \hat{\sigma}_n) \mapsto$ (3.44);
- softening stage:
  - $(\hat{\varepsilon}_{\bar{n}}, \hat{\sigma}_{\bar{n}}) \mapsto$ (3.47)-(3.48);
  - $(\varepsilon_{\rm ult}, 0) \mapsto$ (3.54).

In order to estimate the amount of damage induced by the cracking process in the bar, we introduce a scalar damage variable d, which assumes values in the interval $(0, 1)$: when $d = 0$, the bar is sound, with stiffness modulus $(v_{\rm I}\mathsf{E}_{\rm I}+v_{\rm II}\mathsf{E}_{\rm II})$, and, when $d = 1$, the bar is totally broken, with null stiffness modulus. We refer to the instant at which the n-th crack opens, corresponding to the point $(\hat{\varepsilon}_{n-1}, \check{\sigma}_n)$ in the stress-strain curve of Fig. 8. At this instant, damage d_n (index n specifies that damage corresponds to n cracks) is defined through the stress-strain relation

$$\check{\sigma}_n = (1 - d_n)(v_{\rm I}\mathsf{E}_{\rm I} + v_{\rm II}\mathsf{E}_{\rm II})\varepsilon^{\rm e}_n, \tag{3.60}$$

where $\varepsilon^{\rm e}_n$ is the elastic mean strain, determined by (3.28) and (3.32),

$$\varepsilon^{\rm e}_n = \frac{S(\mathcal{L}_n)}{L}\,\left(c_1(1, \mathcal{L}_n)\hat{\varepsilon}_{n-1} + c_2(n, 1, \mathcal{L}_n, \Delta_{n-1})\right). \tag{3.61}$$

By inverting (3.60), we obtain

$$d_n = 1 - \frac{\check{\sigma}_n}{(v_{\rm I}\mathsf{E}_{\rm I} + v_{\rm II}\mathsf{E}_{\rm II})\varepsilon^{\rm e}_n}. \tag{3.62}$$

In the next examples, damage is evaluated at each new crack opening of the multi-cracking stage.

In addition to damage, we estimate the mean plastic strain as follows

$$p_n = \frac{\sum_{i=1}^{n} \Delta_i}{L}. \tag{3.63}$$

Therefore, in case of unloading, the response is linear elastic, with a global elastic stiffness that decreases as the number of cracks increases according to the stress-strain response (3.60). Moreover, at vanishing stress, a residual strain is observed, given by the sum of all plastic hinges openings divided by the bar length.

The geometrical and constitutive parameters considered in the next examples are taken from [8]. Specifically the bar length is $L = 76\,\text{mm}$, whereas the constitutive parameters are listed at the beginning of Sec. 5, with the exception of $\hat{\Delta}$ and $\check{\Delta}$, which do not enter into the variational model. Here we assume $\hat{\Delta} = \ell_{\rm k}\hat{p} = 0.014\,\text{mm}$, with $\ell_{\rm k}$ and $\hat{p}$ assigned in Sec. 5, and $\check{\Delta} = 0.406\,\text{mm}$, such that the softening modulus approximatively equals the one observed in the tensile experiments in [8]. The value $\hat{\Delta}$ correspond to the stretching of a bar portions between adjacent cracks of length $\ell_{\rm k}$, subjected to the homogeneous plastic strain $\hat{p}$.

3.6.1. Example 1. Equidistant cracks

First, we assume that cracks are always equidistant. This assumption is optimal in terms of strain energy minimization, but it does not satisfy the irreversibility condition for cracks [55]. Indeed, when a new crack forms, the preexisting cracks rearrange their position to satisfy equidistance. For n cracks, the length of each unit-cell is $\ell_n = L/2n$, and (3.29) rewrites

$$S(\mathcal{L}_n) = 2nf(\ell_n), \tag{3.64}$$

with f defined in $(3.27)_2$.

The resulting stress-strain curve is plotted in Fig. 9a, whereas damage and plasticity evolution curves are drawn in Fig. 9b, according to formulas (3.62) and (3.63). Each stress drop in the sawtooth stress-hardening branch corresponds to the opening of a new crack. In Fig. 9a, the crack pattern at each stress-drop is highlighted.

In agreement with experimental evidences, we observe that the frequency of crack opening reduces in the evolution process as the load increases. Consistently, the damage curve considerably increases at the beginning, and progressively reduces its growth rate. Differently, the plastic evolution curve is almost linear in the whole process. Finally, we notice the two different slopes of the linear branch within each tooth of the response curve, which correspond to the cases of a single active hinge and to that of all active hinges.

3.6.2. Example 2. Irreversible cracks.

In this example, crack irreversibility is considered. The strengths of the two phases are randomly perturbed in order to give a realistic description of the cracking process. Unlike the previous example, the cracks positions are not *a-propri* known, nevertheless, the global response, plotted in Fig. 10a, does not differ too much from the curve of the previous example.

In this case, more cracks opens, resulting in a higher damage level, whereas the plastic strain evolution is almost unchanged, Fig. 10b. It can be noticed that, in the hardening stage, the bar exhibits a softer response due to the occurrence of more cracks, with the maximum stress attained for an higher strain value. Moreover, the crack pattern evolution is more irregular, being affected by the random strength perturbation.

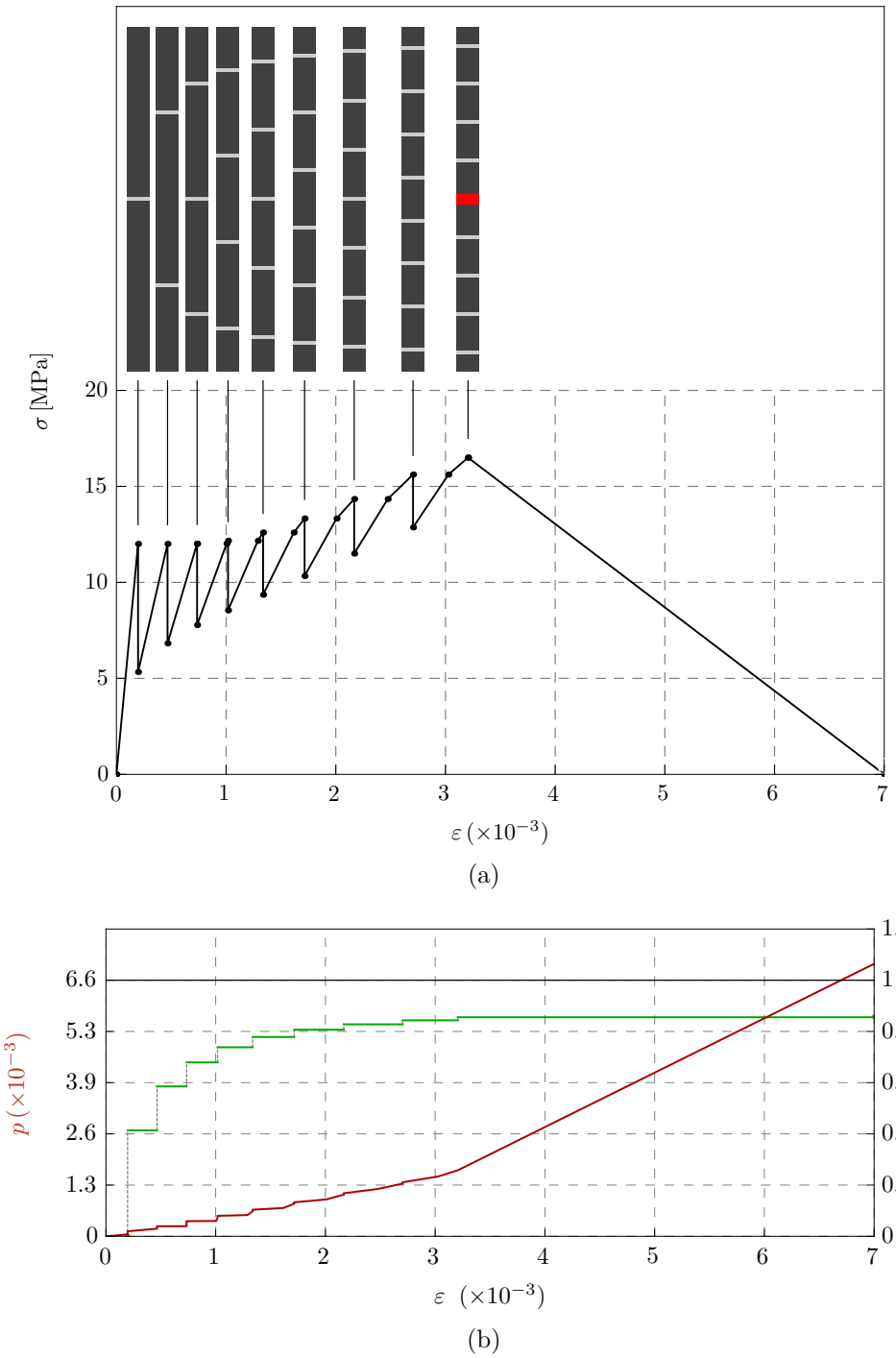

Figure 9: Analytical model without irreversibility condition: (a) Stress-strain curve with corresponding crack pattern evolution; (b) damage and plastic strain curves.

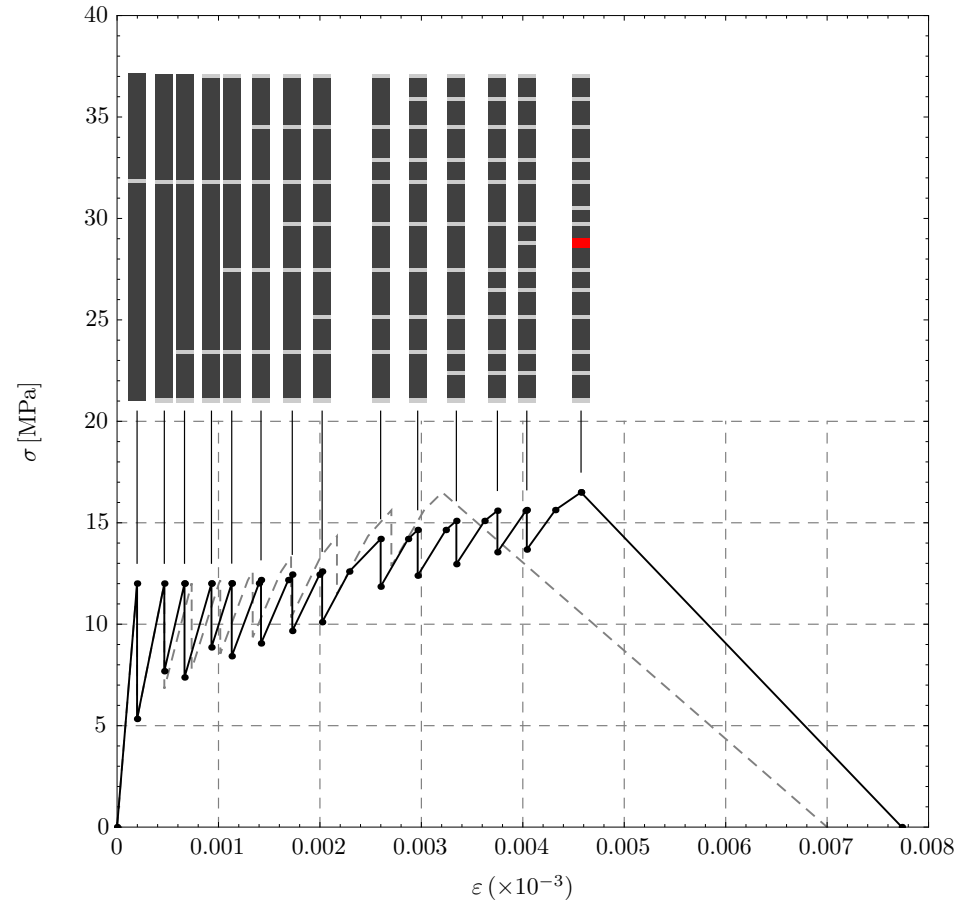

(a)

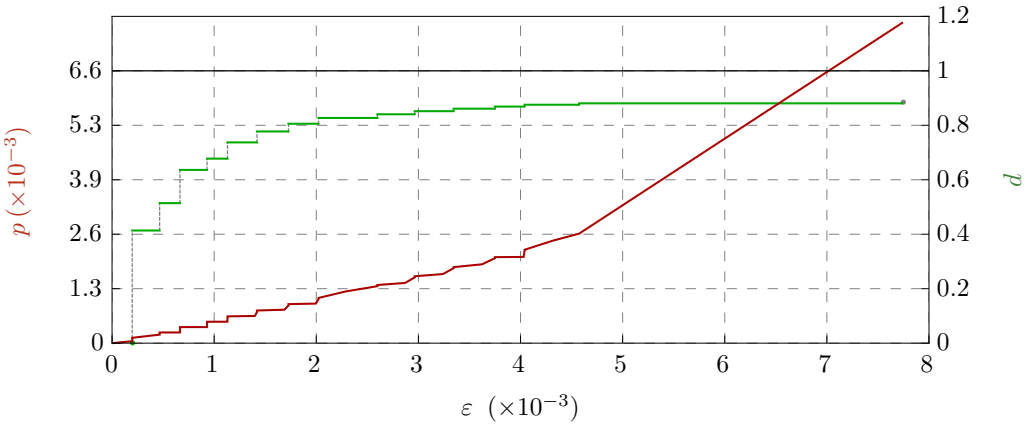

(b)

Figure 10: Analytical model with irreversibility condition: (a) Stress-strain curve with corresponding crack pattern evolution. The dashed gray curve corresponds to the response without crack irreversibility of Fig. 9a; (b) damage and plastic strain curves.

4. Variational model

In this section, a three-dimensional variational model is proposed, based on the scheme of two phases mixture presented in Sec. 2.2. The constitutive assumptions made in Sec. 3.1 for the simple one-dimensional model are extended to the variational three-dimensional context. Thus, as the one-dimensional model, the variational formulation is rate-independent. Fracture and plastic energetic contributions are incorporated into the model to account for cracking of phase I and plastic straining of phase II, and they are enriched by non-local gradient contributions, to avoid energetic costless strain localizations.

4.1. State variables

The displacement fields of the two phases are $\boldsymbol{u}_{\mathrm{I}}$ and $\boldsymbol{u}_{\mathrm{II}}$, and the relative displacement between phases is $\boldsymbol{\delta}$, as in Sec. 2.2. Time-dependent displacements are assigned on a portion of the body boundary

$$\boldsymbol{u}_{\mathrm{I}} = \boldsymbol{u}_{\mathrm{II}} = \boldsymbol{u}_{\mathrm{D}}(t) \text{ on } \partial_{\mathrm{D}}\Omega, \tag{4.1}$$

whereas the complementary boundary part $\partial_{\mathrm{N}}\Omega = \partial\Omega \setminus \partial_{\mathrm{D}}\Omega$ is left stress free. A scalar damage field $d = d(x)$ is defined in phase I, with values in $[0, 1]$. The values $d = 0$ and $d = 1$ correspond to sound and fully damaged material, respectively. To avoid crack healing, damage d must satisfy the irreversibility condition

$$\dot{d} \geq 0. \tag{4.2}$$

Strains of phase II also depend on the plastic strain tensor $\boldsymbol{p} = \boldsymbol{p}(x)$, which is assumed to be symmetric. This assumption allows to reproduce all kinds of fracture mechanisms, including mode I failure mode, which is typically experienced by composites where fibers are randomly oriented within the matrix. Classical plasticity formulations, as Von Mises, are based on the assumption of symmetric and deviatoric plastic strains, describing only mode II and mode III failure mechanisms, characterized by shear bands [56]. The accumulated plastic strain is a scalar history variable defined as

$$\bar{p} := \int_0^t \|\dot{\boldsymbol{p}}(\tau)\| \, \mathrm{d}\tau \tag{4.3}$$

with $\|\cdot\|$ the euclidean norm. The total strains in the two phases are

$$\boldsymbol{\varepsilon}_{\mathrm{I}} = \mathrm{sym}\nabla\boldsymbol{u}_{\mathrm{I}} \quad \text{and} \quad \boldsymbol{\varepsilon}_{\mathrm{II}} = \mathrm{sym}\nabla\boldsymbol{u}_{\mathrm{II}} = \boldsymbol{e} + \boldsymbol{p}. \tag{4.4}$$

Therefore, in phase II, the total strain is decomposed into the sum of elastic strain $\boldsymbol{e} = \boldsymbol{\varepsilon}_{\mathrm{II}} - \boldsymbol{p}$ and plastic strain $\boldsymbol{p}$.

The model state variables are summarized in Tab. 1.

For next developments, it is convenient to collected variables into the vector $\boldsymbol{s} = (\boldsymbol{u}_{\mathrm{I}}, \boldsymbol{u}_{\mathrm{II}}, d, \boldsymbol{p}, \bar{p})$ with $\boldsymbol{s} \in \mathcal{S} = \mathcal{U} \times \mathcal{U} \times [0, 1] \times \mathrm{Sym} \times \mathbb{R}^+$ and $\mathcal{U} = \{\boldsymbol{u} : \boldsymbol{u} = \boldsymbol{u}_{\mathrm{D}}(t) \text{ on } \partial_{\mathrm{D}}\Omega\}$. We assume that $\boldsymbol{s} = \boldsymbol{0}$ at the initial instant $t = 0$.

At a given time t, an admissible perturbation is $\tilde{\boldsymbol{s}} = (\tilde{\boldsymbol{u}}_{\mathrm{I}}, \tilde{\boldsymbol{u}}_{\mathrm{II}}, \tilde{d}, \tilde{\boldsymbol{p}}, \|\tilde{\boldsymbol{p}}\|)$, belonging to the cartesian product $\tilde{\mathcal{S}} = \tilde{\mathcal{U}} \times \tilde{\mathcal{U}} \times \tilde{\mathcal{D}}(d(t)) \times \mathrm{Sym} \times \mathbb{R}^+$, with

$$\tilde{\mathcal{U}} = \{\boldsymbol{u} : \boldsymbol{u} = \boldsymbol{0} \text{ on } \partial_{\mathrm{D}}\Omega\} \quad \text{and} \quad \tilde{\mathcal{D}}(d) = \{f : f \in \mathcal{D} \text{ and } f \geq d\}. \tag{4.5}$$

4.2. Energy

The *total internal energy* of Ω is

$$\mathcal{W}(\boldsymbol{s}) = \int_\Omega v_{\mathrm{I}} w_{\mathrm{I}}(\boldsymbol{u}_{\mathrm{I}}, d) \, \mathrm{d}\Omega + \int_\Omega v_{\mathrm{II}} w_{\mathrm{II}}(\boldsymbol{u}_{\mathrm{II}}, \boldsymbol{p}, \bar{p}) \, \mathrm{d}\Omega + \int_\Omega \frac{1}{2} \frac{\mathsf{E}_{\mathrm{k}}}{\ell_{\mathrm{k}}^2} (\boldsymbol{u}_{\mathrm{I}} - \boldsymbol{u}_{\mathrm{II}})^2 \, \mathrm{d}\Omega. \tag{4.6}$$

phases	state variables	
I (brittle cementitious material)	$\boldsymbol{u}_{\mathrm{I}}$	displacement (*independent*)
	$\boldsymbol{\varepsilon}_{\mathrm{I}}$	infinitesimal total strain
	d	damage (*irreversible*, *independent*)
	∇d	gradient damage
II (ductile fibres)	$\boldsymbol{u}_{\mathrm{II}}$	displacement (*independent*)
	$\boldsymbol{\varepsilon}_{\mathrm{II}}$	infinitesimal total strain
	$\boldsymbol{e}$	elastic strain
	$\boldsymbol{p}$	plastic strain (*independent*)
	$\bar{p}$	accumulated plastic strain (*irreversible*, *history*)
	$\nabla\bar{p}$	gradient plastic strain

Table 1: State variables. Independent sate variables are explicitly indicated.

The first and second contributions are the energies of the brittle phase I and plastic phase II, weighted by their respective volume fractions; the third term is the energy of the linearly elastic bonds between phases, where the elastic coefficient $\mathsf{E}_{\mathrm{k}}/\ell_{\mathrm{k}}^2$ is equal to that of the force-displacement relation (3.8) assumed in the one-dimensional model of Sec. 3. The explicit expressions of the energy densities w_{I}, w_{II} are given in the following.

Energy density w_{I}. For the total internal energy density of the brittle phase I, we consider the expression used in phase-field models of brittle fracture [25]

$$w_{\mathrm{I}}(\boldsymbol{u}_{\mathrm{I}}, d) = \frac{1}{2}\mathsf{g}(d)\,\mathbb{C}_{\mathrm{I}}\boldsymbol{\varepsilon}_{\mathrm{I}}\!:\!\boldsymbol{\varepsilon}_{\mathrm{I}} + \mathsf{w}_{\mathrm{I}}(d) + \frac{1}{2}\overline{\mathsf{w}}_{\mathrm{I}}\ell_{\mathrm{I}}^2\nabla d\cdot\nabla d, \tag{4.7}$$

where the first term is the *elastic strain energy* density, and the second and third terms are the local and non-local *fracture energy* densities, respectively. According to linear elasticity, the elastic term is quadratic with respect to the strain tensor $\boldsymbol{\varepsilon}_{\mathrm{I}}$, with $\mathbb{C}_{\mathrm{I}}$ the elastic strain tensor, and g the *degradation function*, which satisfies the conditions

$$\mathsf{g}'(d) \le 0, \quad \mathsf{g}(0) = 1, \quad \mathsf{g}(1) = 0. \tag{4.8}$$

Since g decreases to zero as d increases, material stiffness reduces when damage advances, until it nullifies for $d = 1$. The fracture energy is sum of a local and a non-local term, depending on d and ∇d, respectively. Following [25], we assume that w_{I} satisfies the conditions

$$\mathsf{w}_{\mathrm{I}}(0) = 0, \quad \mathsf{w}_{\mathrm{I}}'(0) = \overline{\mathsf{w}}_{\mathrm{I}} > 0, \quad \mathsf{w}_{\mathrm{I}}'(d) \ge 0, \tag{4.9}$$

where the second condition allows for an initial phase of elastic deformation, without any damage, as shown later on. The assumption of non-decreasing w_{I} implies that

$$\dot{\mathsf{w}}_{\mathrm{I}}(d) = \mathsf{w}_{\mathrm{I}}'(d)\,\dot{d} \ge 0, \tag{4.10}$$

and, thus, that the local fracture energy is dissipative. The non-local gradient contribution (third term in (4.7)) introduces the internal length ℓ_{I} related to the size of the zone where d localizes at crack, also called process-zone. Here $\mathbb{C}_{\mathrm{I}}$ and w_{I} are left unspecified to leave the model as general as possible, but specific shapes will be assigned in Sec. 4.6, and used in numerical simulations in Sec. 5.

The total internal energy density w_{II}. The energy density assigned to phase II is

$$w_{\mathrm{II}}(\boldsymbol{u}_{\mathrm{II}}, \boldsymbol{p}, \bar{p}) = \frac{1}{2}\mathbb{C}_{\mathrm{II}}(\boldsymbol{\varepsilon}_{\mathrm{II}} - \boldsymbol{p})\!:\!(\boldsymbol{\varepsilon}_{\mathrm{II}} - \boldsymbol{p}) + \mathsf{w}_{\mathrm{II}}(\bar{p}) + \frac{1}{2}\overline{\mathsf{w}}_{\mathrm{II}}\ell_{\mathrm{II}}^2\nabla\bar{p}\cdot\nabla\bar{p}, \tag{4.11}$$

where the first term is the elastic energy density, which depends on the elastic part of the strain tensor $\boldsymbol{e} = \boldsymbol{\varepsilon}_{\mathrm{II}} - \boldsymbol{p}$, and the second and third terms are the local and nonlocal plastic energy densities, functions of the accumulated plastic strain $\bar{p}$ and $\nabla\bar{p}$, respectively. The elastic energy is a quadratic form, with $\mathbb{C}_{\mathrm{II}}$ the elasticity tensor, and the plastic energy density w_{II} satisfies the conditions

$$\mathsf{w}_{\mathrm{II}}(0) = 0, \quad \mathsf{w}'_{\mathrm{II}}(\bar{p}) > 0. \tag{4.12}$$

Since

$$\dot{\mathsf{w}}_{\mathrm{II}}(\bar{p}) = \mathsf{w}'_{\mathrm{II}}(\bar{p})\,\dot{\bar{p}} = \mathsf{w}'_{\mathrm{II}}(\bar{p})\,\|\dot{\boldsymbol{p}}\| \geq 0, \tag{4.13}$$

w_{II} is also dissipative. As shown in [41, 43, 33], the plastic response strongly depends on the convexity properties of w_{II}. Indeed, in case of convex w_{II}, plastic strains tend to diffuse within the body in a regime of stress-hardening. On the contrary, if w_{II} is sufficiently concave, plastic strains localize in small portions of the body in regime of stress-softening. In the latter situation, the non-local energy term plays the role of localization limiter, penalizing plastic strain gradients. To this end, the internal length parameter ℓ_{II} influences the size of the localization zone. In Sec. 4.6, a specific expression for w_{II} is assumed, and rules to calibrate the parameters are proposed.

The energy density (4.11) is typical of Aifantis's gradient plasticity theory [47, 48], reformulated in a thermodynamically consistent format in [57, 58], and discussed in [59, Sec. 89], with particular emphasis on the dissipative and stored nature of local and non-local plasticity contributions.

Stress tensors $\boldsymbol{\sigma}_{\mathrm{I}}$ and $\boldsymbol{\sigma}_{\mathrm{II}}$ of phases I and II are obtained by differentiating the phases elastic energy densities with respect to the corresponding elastic strains. Similarly, the relative force $\boldsymbol{\tau}$ results from differentiation of the bond energy density with respect to the relative displacement $(\boldsymbol{u}_{\mathrm{I}} - \boldsymbol{u}_{\mathrm{II}})$. Their expressions are

$$\boldsymbol{\sigma}_{\mathrm{I}} = \mathsf{g}(d)\mathbb{C}_{\mathrm{I}}\boldsymbol{\varepsilon}_{\mathrm{I}}, \qquad \boldsymbol{\sigma}_{\mathrm{II}} = \mathbb{C}_{\mathrm{II}}\left(\boldsymbol{\varepsilon}_{\mathrm{II}} - \boldsymbol{p}\right), \qquad \boldsymbol{\tau} = \frac{\mathsf{E}_{\mathrm{k}}}{\ell_{\mathrm{k}}^2}(\boldsymbol{u}_{\mathrm{I}} - \boldsymbol{u}_{\mathrm{II}}). \tag{4.14}$$

By inverting $(4.14)_{1,2}$, we obtain the inverse relations

$$\boldsymbol{\varepsilon}_{\mathrm{I}} = \frac{1}{\mathsf{g}(d)}\mathbb{S}_{\mathrm{I}}\boldsymbol{\sigma}_{\mathrm{I}}, \qquad \boldsymbol{\varepsilon}_{\mathrm{II}} = \mathbb{S}_{\mathrm{II}}\boldsymbol{\sigma}_{\mathrm{II}} + \boldsymbol{p}, \tag{4.15}$$

where $\mathbb{S}_{\mathrm{I}} = \mathbb{C}_{\mathrm{I}}^{-1}$ and $\mathbb{S}_{\mathrm{II}} = \mathbb{C}_{\mathrm{II}}^{-1}$ are the compliance tensors of phases I and II, respectively.

4.3. Energetic formulation

According to the energetic formulation for rate independent systems [22], the evolution process is governed by three principles: the *stability condition*, the *energy balance*, and the *dissipation inequality*.

4.3.1. Stability condition

We consider a *local directional stability condition*, which states that a process $\boldsymbol{s}(t)$ is stable if at any time $t \in [0, T]$ and $\forall \tilde{\boldsymbol{s}} \in \tilde{\mathcal{S}}$, $\exists \bar{h} > 0 : \forall h \in [0, \bar{h}]$

$$\mathcal{W}(\boldsymbol{s}) \leq \mathcal{W}(\boldsymbol{s} + h\tilde{\boldsymbol{s}}) \tag{ST}$$

For the Gâteaux differentiable total energy (4.6), a necessary condition for (ST) is the first variation of $\mathcal{W}$ to be non negative for any admissible perturbation, namely

$$D\mathcal{W}(\boldsymbol{s})[\tilde{\boldsymbol{s}}] \geq 0, \qquad \forall \tilde{\boldsymbol{s}} \in \tilde{\mathcal{S}}. \tag{4.16}$$

The above first-order stability condition is an equilibrium equation, and its solutions are equilibrium configurations.[4] By substituting (4.6) into (4.16) and integrating by parts, we obtain

$$\begin{aligned}
&\int_\Omega \left((-v_{\mathrm{I}} \operatorname{div} \boldsymbol{\sigma}_{\mathrm{I}} + \boldsymbol{\tau}) \cdot \tilde{\boldsymbol{u}}_{\mathrm{I}} + (-v_{\mathrm{II}} \operatorname{div} \boldsymbol{\sigma}_{\mathrm{II}} - \boldsymbol{\tau}) \cdot \tilde{\boldsymbol{u}}_{\mathrm{II}} \right) \mathrm{d}\Omega + \\
&+ \int_\Omega v_{\mathrm{I}} \left(\frac{1}{2} \frac{\mathsf{g}'(d)}{\mathsf{g}^2(d)} \, \mathbb{S}_{\mathrm{I}} \boldsymbol{\sigma}_{\mathrm{I}} : \boldsymbol{\sigma}_{\mathrm{I}} + \mathsf{w}_{\mathrm{I}}'(d) - \overline{\mathsf{w}}_{\mathrm{I}} \ell_{\mathrm{I}}^2 \Delta d \right) \tilde{d} \, \mathrm{d}\Omega + \\
&+ \int_\Omega v_{\mathrm{II}} \left(-\boldsymbol{\sigma}_{\mathrm{I}} : \tilde{\boldsymbol{p}} + \left(\mathsf{w}_{\mathrm{II}}'(\bar{p}) - \overline{\mathsf{w}}_{\mathrm{II}} \ell_{\mathrm{II}}^2 \Delta \bar{p} \right) \|\tilde{\boldsymbol{p}}\| \right) \mathrm{d}\Omega \\
&+ \int_{\partial_{\mathrm{N}}\Omega} (v_{\mathrm{I}} \boldsymbol{\sigma}_{\mathrm{I}} \boldsymbol{n} \cdot \tilde{\boldsymbol{u}}_{\mathrm{I}} + v_{\mathrm{II}} \boldsymbol{\sigma}_{\mathrm{II}} \boldsymbol{n} \cdot \tilde{\boldsymbol{u}}_{\mathrm{II}}) \, \mathrm{d}\partial\Omega \\
&+ \int_{\partial\Omega} (v_{\mathrm{I}} \overline{\mathsf{w}}_{\mathrm{I}} \ell_{\mathrm{I}}^2 \nabla d \cdot \boldsymbol{n} \tilde{d} + v_{\mathrm{II}} \overline{\mathsf{w}}_{\mathrm{II}} \ell_{\mathrm{II}}^2 \nabla \bar{p} \cdot \boldsymbol{n} \|\tilde{\boldsymbol{p}}\|) \, \mathrm{d}\partial\Omega \geq 0, \qquad \forall \tilde{\boldsymbol{s}} \in \tilde{\mathcal{S}},
\end{aligned} \tag{4.17}$$

which, by standard arguments of calculus of variations, leads to the following equations:

1. *Equilibrium equations*

$$v_{\mathrm{I}} \operatorname{div} \boldsymbol{\sigma}_{\mathrm{I}} - \boldsymbol{\tau} = \boldsymbol{0}, \quad v_{\mathrm{II}} \operatorname{div} \boldsymbol{\sigma}_{\mathrm{II}} + \boldsymbol{\tau} = \boldsymbol{0}, \quad \text{in } \Omega, \tag{4.18}$$

and *macroscopic boundary conditions*

$$\boldsymbol{\sigma}_{\mathrm{I}} \boldsymbol{n} = \boldsymbol{\sigma}_{\mathrm{II}} \boldsymbol{n} = \boldsymbol{0}, \quad \text{on } \partial_{\mathrm{N}}\Omega. \tag{4.19}$$

2. *Damage threshold condition* for phase I

$$f_{\mathrm{I}}(\boldsymbol{\sigma}_{\mathrm{I}}, d, \Delta d) := -\frac{1}{2} \frac{\mathsf{g}'(d)}{\mathsf{g}^2(d)} \, \mathbb{S}_{\mathrm{I}} \boldsymbol{\sigma}_{\mathrm{I}} : \boldsymbol{\sigma}_{\mathrm{I}} - \mathsf{w}_{\mathrm{I}}'(d) + \overline{\mathsf{w}}_{\mathrm{I}} \ell_{\mathrm{I}}^2 \Delta d \leq 0, \quad \text{in } \Omega, \tag{4.20}$$

and *damage boundary conditions*

$$\nabla d \cdot \boldsymbol{n} \geq 0, \quad \text{on } \partial\Omega. \tag{4.21}$$

3. *Plasticity yield condition* for phase II

$$f_{\mathrm{II}}(\boldsymbol{\sigma}_{\mathrm{II}}, \bar{p}, \Delta\bar{p}) := \|\boldsymbol{\sigma}_{\mathrm{II}}\| - \mathsf{w}_{\mathrm{II}}'(\bar{p}) + \overline{\mathsf{w}}_{\mathrm{II}} \ell_{\mathrm{II}}^2 \Delta\bar{p} \leq 0, \quad \text{in } \Omega, \tag{4.22}$$

and *plasticity boundary conditions*

$$\nabla \bar{p} \cdot \boldsymbol{n} \geq 0, \quad \text{on } \partial\Omega. \tag{4.23}$$

It is worth noting that the relations $f_{\mathrm{I}} = 0$ and $f_{\mathrm{II}} = 0$ define the boundaries of the elastic domains for each material phase, which are spheres in the principal stresses space.

4.3.2. Energy balance

Descending from the first principle of thermodynamics, the energy balance states that for any time-instant $t \in [0, T]$

$$\mathcal{W}(\boldsymbol{s}(t)) - \mathcal{W}(\boldsymbol{0}) - \mathcal{L}(t) = 0, \tag{EB}$$

[4] In addition to (4.16), higher-order stability conditions needs to be assigned in order to obtain sufficient conditions for the stability notion (ST), [23].

where $\mathcal{L}(t)$ is the external work expended in the time interval $[0,t]$. In case of the proposed model, since body and external loads are null, the external work is only due to the assigned displacement $\bar{\boldsymbol{u}}(t)$ on $\partial_{\mathrm{D}}\Omega$. It is

$$\mathcal{L}(t) = \int_0^t \left(\int_{\partial_{\mathrm{D}}\Omega} (v_{\mathrm{I}} \boldsymbol{f}_{\mathrm{I}} + v_{\mathrm{II}} \boldsymbol{f}_{\mathrm{II}}) \cdot \dot{\bar{\boldsymbol{u}}}(t) \, \mathrm{d}\partial\Omega \right) \mathrm{d}\tau, \tag{4.24}$$

with $\boldsymbol{f}_{\mathrm{I}} = \boldsymbol{\sigma}_{\mathrm{I}} \boldsymbol{n}$ and $\boldsymbol{f}_{\mathrm{II}} = \boldsymbol{\sigma}_{\mathrm{II}} \boldsymbol{n}$ being the reaction stresses of the two phases.

For time-differentiable energies, equation (EB) can be replaced by the following equation of energy rates balance

$$\dot{\mathcal{W}}(\boldsymbol{s}(t)) - \dot{\mathcal{L}}(t) = 0. \tag{eb}$$

Substituting (4.6) and (4.24) into (eb), and integrating by parts, we obtain

$$\begin{aligned}
&\int_\Omega \left((-v_{\mathrm{I}} \operatorname{div} \boldsymbol{\sigma}_{\mathrm{I}} + \boldsymbol{\tau}) \cdot \dot{\boldsymbol{u}}_{\mathrm{I}} + (-v_{\mathrm{II}} \operatorname{div} \boldsymbol{\sigma}_{\mathrm{II}} - \boldsymbol{\tau}) \cdot \dot{\boldsymbol{u}}_{\mathrm{II}} \right) \mathrm{d}\Omega + \\
&+ \int_{\partial_{\mathrm{N}}\Omega} (v_{\mathrm{I}} \boldsymbol{\sigma}_{\mathrm{I}} \boldsymbol{n} \cdot \dot{\boldsymbol{u}}_{\mathrm{I}} + v_{\mathrm{II}} \boldsymbol{\sigma}_{\mathrm{II}} \boldsymbol{n} \cdot \dot{\boldsymbol{u}}_{\mathrm{II}}) \, \mathrm{d}\partial\Omega \\
&+ \int_\Omega v_{\mathrm{I}} \left(\frac{1}{2} \frac{\mathsf{g}'(d)}{(\mathsf{g}(d))^2} \mathbb{S}_{\mathrm{I}} \boldsymbol{\sigma}_{\mathrm{I}} : \boldsymbol{\sigma}_{\mathrm{I}} + \mathsf{w}_{\mathrm{I}}'(d) - \overline{\mathsf{w}}_{\mathrm{I}} \ell_{\mathrm{I}}^2 \Delta d \right) \dot{d} \, \mathrm{d}\Omega + \\
&+ \int_\Omega v_{\mathrm{II}} \left(-\boldsymbol{\sigma}_{\mathrm{II}} : \dot{\boldsymbol{p}} + \left(\mathsf{w}_{\mathrm{II}}'(\bar{p}) - \overline{\mathsf{w}}_{\mathrm{II}} \ell_{\mathrm{II}}^2 \Delta \bar{p} \right) \|\dot{\boldsymbol{p}}\| \right) \mathrm{d}\Omega \\
&+ \int_{\partial\Omega} (v_{\mathrm{I}} \overline{\mathsf{w}}_{\mathrm{I}} \ell_{\mathrm{I}}^2 \nabla d \cdot \boldsymbol{n} \, \dot{d} + v_{\mathrm{II}} \overline{\mathsf{w}}_{\mathrm{II}} \ell_{\mathrm{II}}^2 \nabla \bar{p} \cdot \boldsymbol{n} \, \|\dot{\boldsymbol{p}}\|) \, \mathrm{d}\partial\Omega = 0.
\end{aligned} \tag{4.25}$$

First and second integrals are null by (4.18) and (4.19). The remaining integrals are non-negative by (4.2) and inequalities (4.20)-(4.23), and, as a result, their integrands must vanish. By nullifying the third integral, we obtain the following consistency condition for damage

$$\left(-\frac{1}{2} \frac{\mathsf{g}'(d)}{(\mathsf{g}(d))^2} \mathbb{S}_{\mathrm{I}} \boldsymbol{\sigma}_{\mathrm{I}} : \boldsymbol{\sigma}_{\mathrm{I}} - \mathsf{w}_{\mathrm{I}}'(d) + \overline{\mathsf{w}}_{\mathrm{I}} \ell_{\mathrm{I}}^2 \Delta d \right) \dot{d} = f_{\mathrm{I}}(\boldsymbol{\sigma}_{\mathrm{I}}, d, \Delta d) \dot{d} = 0, \tag{4.26}$$

which states that the yield function f_{I} must maintains equal to zero when damage evolves. By requiring the fourth integral to be null, we get the plastic consistency condition

$$\left(\|\boldsymbol{\sigma}_{\mathrm{II}}\| - \mathsf{w}_{\mathrm{II}}'(\bar{p}) + \overline{\mathsf{w}}_{\mathrm{II}} \ell_{\mathrm{II}}^2 \Delta \bar{p} \right) \|\dot{\boldsymbol{p}}\| = f_{\mathrm{II}}(\boldsymbol{\sigma}_{\mathrm{II}}, \bar{p}, \Delta \bar{p}) \|\dot{\boldsymbol{p}}\| = 0, \tag{4.27}$$

and the plastic flow rule

$$\dot{\boldsymbol{p}} = \dot{\bar{p}} \, \boldsymbol{n}_{\mathrm{II}}, \quad \text{with} \quad \boldsymbol{n}_{\mathrm{II}} = \frac{\boldsymbol{\sigma}_{\mathrm{II}}}{\|\boldsymbol{\sigma}_{\mathrm{II}}\|} \left(= \frac{\partial f_{\mathrm{II}}}{\partial \boldsymbol{\sigma}_{\mathrm{II}}} \right), \tag{4.28}$$

which accounts for associative plasticity. Finally, the last boundary integral in (4.25) nullifies if the following boundary conditions are satisfied

$$\nabla d \cdot \boldsymbol{n} = 0, \quad \text{and} \quad \nabla \bar{p} \cdot \boldsymbol{n} = 0, \qquad \text{on } \partial\Omega. \tag{4.29}$$

It is worth noting that boundary conditions for the internal variables automatically descend from the variational problem and do not have to be prescribed *a-priori* as in standard formulations.

Remark. Energy balance for time-discontinuous evolutions. As highlighted in [23], within the framework of rate-independent processes, energy balance at time instants where a discontinuous evolution occur is at least arguable if not wrong. Therefore, it is often more reasonable to ensure only an energy imbalance at such discontinuous instants, with possibly a criterion for guiding the time discontinuous transition as a gradient flow law or a vanishing viscosity contribution.

4.3.3. Dissipation inequality

The dissipation inequality for isothermal processes states that

$$\mathcal{D} = \mathcal{P} - \dot{\mathcal{H}} \geq 0 \tag{4.30}$$

where $\mathcal{D}$ is the local dissipated power, $\mathcal{P}$ is the local mechanical internal power, and $\mathcal{H}$ is the free energy density. The expression of the free energy density is

$$\begin{aligned} \mathcal{H} = \; & v_{\mathrm{I}} \left(\frac{1}{2} \mathsf{g}(d)\, \mathbb{C}_{\mathrm{I}} \boldsymbol{\varepsilon}_{\mathrm{I}} : \boldsymbol{\varepsilon}_{\mathrm{I}} + \frac{1}{2} \overline{\mathsf{w}}_{\mathrm{I}} \ell_{\mathrm{I}}^2 \nabla d \cdot \nabla d \right) + \\ & + v_{\mathrm{II}} \left(\frac{1}{2} \mathbb{C}_{\mathrm{II}} (\boldsymbol{\varepsilon}_{\mathrm{II}} - \boldsymbol{p}) : (\boldsymbol{\varepsilon}_{\mathrm{II}} - \boldsymbol{p}) + \frac{1}{2} \overline{\mathsf{w}}_{\mathrm{II}} \ell_{\mathrm{II}}^2 \nabla \bar{p} \cdot \nabla \bar{p} \right) + \\ & + \frac{1}{2} \frac{\mathsf{E}_{\mathrm{k}}}{\ell_{\mathrm{k}}^2} (\boldsymbol{u}_{\mathrm{I}} - \boldsymbol{u}_{\mathrm{II}})^2, \end{aligned} \tag{4.31}$$

which is sum of the elastic energy densities of the two phases, the non-local damage and plastic energy densities, and the bonds elastic energy. Local damage and plastic energies are not included into the free energy since they are dissipative potentials, as shown by inequalities (4.10) and (4.13) and extensively discussed in [35]. The local internal mechanical power is

$$\mathcal{P} = v_{\mathrm{I}}\, \boldsymbol{\sigma}_{\mathrm{I}} : \dot{\boldsymbol{\varepsilon}}_{\mathrm{II}} + v_{\mathrm{II}}\, \boldsymbol{\sigma}_{\mathrm{II}} : \dot{\boldsymbol{\varepsilon}}_{\mathrm{II}} + \boldsymbol{\tau} \cdot (\dot{\boldsymbol{u}}_{\mathrm{I}} - \dot{\boldsymbol{u}}_{\mathrm{II}}). \tag{4.32}$$

Then, using the definitions (4.14) for the stresses $\boldsymbol{\sigma}_{\mathrm{I}}$ and $\boldsymbol{\sigma}_{\mathrm{II}}$, and the force $\boldsymbol{\tau}$, and the boundary conditions (4.29), we get

$$\mathcal{D} = -v_{\mathrm{I}} \left(\frac{1}{2} \frac{\mathsf{g}'(d)}{\mathsf{g}(d)^2}\, \mathbb{S}_{\mathrm{I}} \boldsymbol{\sigma}_{\mathrm{I}} : \boldsymbol{\sigma}_{\mathrm{I}} - \overline{\mathsf{w}}_{\mathrm{I}} \ell_{\mathrm{I}}^2 \Delta d \right) \dot{d} - v_{\mathrm{II}} \left(-\boldsymbol{\sigma}_{\mathrm{II}} : \dot{\boldsymbol{p}} - \overline{\mathsf{w}}_{\mathrm{II}} \ell_{\mathrm{II}}^2 \Delta \bar{p}\, \|\dot{\boldsymbol{p}}\| \right) \geq 0, \tag{4.33}$$

which is always satisfied. Indeed, by considering (4.10), (4.13), (4.26) and (4.27), the dissiaption (4.33) reduces to

$$\mathcal{D} = \mathsf{w}_{\mathrm{I}}'(d)\, \dot{d} + \mathsf{w}_{\mathrm{II}}'(\bar{p})\, \dot{\bar{p}} \geq 0 \tag{4.34}$$

which is always non-negative.

4.4. Time discrete scheme for the evolution problem

In this section, a time discrete evolution scheme is presented, which is used in the finite element numerical implementation of the variational model. In the following, index t refers to time instant.

Time is discretized into intervals of finite size δt. Given the solution $\boldsymbol{s}_t = (\boldsymbol{u}_{\mathrm{I}\,t}, \boldsymbol{u}_{\mathrm{II}\,t}, d_t, \boldsymbol{p}_t, \bar{p}_t)$ at instant t, the scheme provides an iterative procedure to estimate the increment $\delta \boldsymbol{s}_t$, which allows to determine the solution $\boldsymbol{s}_{t+\delta t} = \boldsymbol{s}_t + \delta \boldsymbol{s}_t$ at the instant $t + \delta t$.

Within the iterative procedure, the increment of the plastic strain tensor is approximated by $\delta \boldsymbol{p} = \delta \bar{p}\, \boldsymbol{n}_{\mathrm{II}}$, where $\boldsymbol{n}_{\mathrm{II}}$ is the flow tensor evaluated at the previous numerical integration step. Accordingly, the list of unknown increments reduces to $\delta \boldsymbol{q} = (\delta \boldsymbol{u}_{\mathrm{I}}, \delta \boldsymbol{u}_{\mathrm{II}}, \delta d, \delta \bar{p})$. The numerical implementation consists in solving a sequence of minimum problems, which operate on the second-order development of energy (4.6)

$$\mathcal{W}(\boldsymbol{s} + \delta \boldsymbol{s}) = \mathcal{W}(\boldsymbol{s}) + \delta \mathcal{W}(\boldsymbol{s})[\delta \boldsymbol{s}] + \frac{1}{2} \delta^2 \mathcal{W}(\boldsymbol{s})[\delta \boldsymbol{s}] \cdot \delta \boldsymbol{s} = \mathcal{W}(\boldsymbol{s}) + \mathcal{F}(\boldsymbol{s};\, \delta \boldsymbol{q}), \tag{4.35}$$

with

$$
\begin{aligned}
&\mathcal{F}(\boldsymbol{s};\,\delta\boldsymbol{q}) = \mathcal{F}(\boldsymbol{u}_{\rm I},\boldsymbol{u}_{\rm II},d,\boldsymbol{p},\bar{p}\,;\delta\boldsymbol{u}_{\rm I},\delta\boldsymbol{u}_{\rm II},\delta d,\delta\bar{p}) = \\
&\int_\Omega \Bigg\{ v_{\rm I}\left[\frac{1}{2}\mathsf{g}(d)\mathbb{C}_{\rm I}\delta\boldsymbol{\varepsilon}_{\rm I}\!:\!\delta\boldsymbol{\varepsilon}_{\rm I} + \mathsf{g}'(d)\boldsymbol{\sigma}_{\rm I}\!:\!\delta\boldsymbol{\varepsilon}_{\rm I}\delta d + \frac{1}{4}\mathsf{g}''(d)\boldsymbol{\sigma}_{\rm I}\!:\!\boldsymbol{\varepsilon}_{\rm I}\delta d^2 + \frac{1}{2}\mathsf{w}_{\rm I}''(d)\delta d^2 + \frac{1}{2}\overline{\mathsf{w}}_{\rm I}\ell_{\rm I}^2\nabla\delta d\cdot\nabla\delta d\right] + \\
&+v_{\rm II}\left[\frac{1}{2}\mathbb{C}_{\rm II}\delta\boldsymbol{\varepsilon}_{\rm II}\!:\!\delta\boldsymbol{\varepsilon}_{\rm II} - \mathbb{C}_{\rm II}\boldsymbol{n}_{\rm II}\!:\!\delta\boldsymbol{\varepsilon}_{\rm II}\delta\bar{p} + \frac{1}{2}\mathbb{C}_{\rm II}\boldsymbol{n}_{\rm II}\!:\!\boldsymbol{n}_{\rm II}\delta\bar{p}^2 + \frac{1}{2}\mathsf{w}_{\rm II}''(\bar{p})\delta\bar{p}^2 + \frac{1}{2}\overline{\mathsf{w}}_{\rm II}\ell_{\rm II}^2\nabla\delta\bar{p}\cdot\nabla\delta\bar{p}\right] + \\
&+\frac{1}{2}\frac{\mathsf{E}_{\rm k}}{\ell_{\rm k}^2}(\delta\boldsymbol{u}_{\rm I}-\delta\boldsymbol{u}_{\rm II})^2\Bigg\}\,d\Omega + \\
&+\int_\Omega \Bigg\{ v_{\rm I}\left[\mathsf{g}(d)\boldsymbol{\sigma}_{\rm I}\!:\!\delta\boldsymbol{\varepsilon}_{\rm I} + \frac{1}{2}\mathsf{g}'(d)\boldsymbol{\sigma}_{\rm I}\!:\!\boldsymbol{\varepsilon}_{\rm I}\delta d + \mathsf{w}_{\rm I}'(d)\delta d + \overline{\mathsf{w}}_{\rm I}\ell_{\rm I}^2\nabla d\cdot\nabla\delta d\right] + \\
&+v_{\rm II}\left[\boldsymbol{\sigma}_{\rm II}\!:\!(\delta\boldsymbol{\varepsilon}_{\rm II}-\boldsymbol{n}_{\rm II}\delta\bar{p}) + \mathsf{w}_{\rm II}'(\bar{p})\delta\bar{p} + \overline{\mathsf{w}}_{\rm II}\ell_{\rm II}^2\nabla\bar{p}\cdot\nabla\delta\bar{p}\right] + \boldsymbol{\tau}(\delta\boldsymbol{u}_{\rm I}-\delta\boldsymbol{u}_{\rm II})\Big\}\,d\Omega\,.
\end{aligned}
\tag{4.36}
$$

The flowchart of the iterative procedure that allows to estimate the solution within a time step $t \to t+\delta t$ is outlined in the following. Apices i and j refer to iteration steps within the iterative loops of the scheme. The solution $\boldsymbol{s}_t$ is supposed to be known, and $\boldsymbol{s}_{t+\delta t}$ is to be determined.

1. Initialize $\boldsymbol{s}^0 = \boldsymbol{s}_t$.
2. **Loop 1** $\rightarrow$ to estimate $(\boldsymbol{u}_{\rm I}, \boldsymbol{u}_{\rm II}, d)$.
   ***i*-th iteration**
   - Determine $(\delta\boldsymbol{u}_{\rm I}^i, \delta\boldsymbol{u}_{\rm II}^i) = \arg\min_{(\delta\boldsymbol{u}_{\rm I},\delta\boldsymbol{u}_{\rm II})} \mathcal{F}(\mathbf{s}^{i-1},\,\delta\mathbf{q})$.
   - Update the displacements $\boldsymbol{u}_{\rm I}^i = \boldsymbol{u}_{\rm I}^{i-1} + \delta\boldsymbol{u}_{\rm I}^i$, $\boldsymbol{u}_{\rm II}^i = \boldsymbol{u}_{\rm II}^{i-1} + \delta\boldsymbol{u}_{\rm II}^i$.
   - Update the solution $\mathbf{s}^i = (\boldsymbol{u}_{\rm I}^i, \boldsymbol{u}_{\rm II}^i, d^{i-1}, \boldsymbol{p}^0, \bar{p}^0)$.
   - Determine $\delta d^i = \arg\min_{\delta d} \mathcal{F}(\mathbf{s}^i,\,\delta\mathbf{q})$, with constraint $\delta d \geq d_t - d^{i-1}$.
   - Update the $d^i = d^{i-1} + \delta d^i$.
   - Update the solution $\mathbf{s}^i = (\boldsymbol{u}_{\rm I}^i, \boldsymbol{u}_{\rm II}^i, d^i, \boldsymbol{p}^0, \bar{p}^0)$.
   - End loop when $|\delta d^i|_{L_1} \leq \mathrm{toll}_d$.
3. Initialize $\boldsymbol{s}^0 = \boldsymbol{s}^i$
4. **Loop 2** $\rightarrow$ to estimate $(\boldsymbol{u}_{\rm I}, \boldsymbol{u}_{\rm II}, \boldsymbol{p}, \bar{p})$.
   ***j*-th iteration**
   - Determine $(\delta\boldsymbol{u}_{\rm I}^j, \delta\boldsymbol{u}_{\rm II}^j) = \arg\min_{(\delta\boldsymbol{u}_{\rm I},\delta\boldsymbol{u}_{\rm II})} \mathcal{F}(\mathbf{s}^{j-1},\,\delta\mathbf{q})$.
   - Update the displacements $\boldsymbol{u}_{\rm I}^j = \boldsymbol{u}_{\rm I}^{j-1} + \delta\boldsymbol{u}_{\rm I}^j$, $\boldsymbol{u}_{\rm II}^j = \boldsymbol{u}_{\rm II}^{j-1} + \delta\boldsymbol{u}_{\rm II}^j$.
   - Update the solution $\mathbf{s}^j = (\boldsymbol{u}_{\rm I}^j, \boldsymbol{u}_{\rm II}^j, d^0, \boldsymbol{p}^{j-1}, \bar{p}^{j-1})$.
   - Determine $\delta\bar{p}^j = \arg\min_{\delta\bar{p}} \mathcal{F}(\mathbf{s}^j,\,\delta\mathbf{q})$, under the constraint $\delta\bar{p} \geq \bar{p}_t - \bar{p}^{j-1}$.
   - Update the cumulated plastic strain $\bar{p}^j = \bar{p}^{j-1} + \delta\bar{p}^j$.
   - Update the stress tensor $\boldsymbol{\sigma}_{\rm II}^j = \mathbb{C}_{\rm II}\left[\mathrm{sym}\nabla\boldsymbol{u}_{\rm II}^j - \left(\boldsymbol{p}_t + \left(\bar{p}^j - \bar{p}_t\right)\boldsymbol{n}_{\rm II}^{j-1}\right)\right]$, flow tensor $\boldsymbol{n}_{\rm II}^j = \boldsymbol{\sigma}_{\rm II}^j/\|\boldsymbol{\sigma}_{\rm II}^j\|$, and the plastic strain tensor $\boldsymbol{p}^j = \boldsymbol{p}_t + \left(\bar{p}^j - \bar{p}_t\right)\boldsymbol{n}_{\rm II}^j$.
   - Update the solution $\mathbf{s}^j = (\boldsymbol{u}_{\rm I}^j, \boldsymbol{u}_{\rm II}^j, d^0, \boldsymbol{p}^j, \bar{p}^j)$.
   - End loop when $|\delta\bar{p}^i|_{L_1} \leq \mathrm{toll}_{\bar{p}}$.
5. Set $\mathbf{s}_{t+\delta t} = \mathbf{s}^j$ and pass to the next time step.

All minimum problems operate on convex quadratic functionals, and problems for δd and $\delta\bar{p}$ are constrained by linear inequalities. Discretized by finite elements, they turn into quadratic programming problems, which are solved numerically. Numerical tests have shown that the two loops converge after few iterations. The double loops have been also iterated with the aim of improving accuracy. Since it was found that multiple iterations do not considerably improve solution accuracy, the above listed two loops 1 and 2 are performed one time per time step, in order to save computational cost.

4.5. 1D variational model

The equations deduced in the previous sections are specialized to the case of a one-dimensional tensile bar. The one-dimensional problem provides simple formulas relating model constitutive parameters to quantities which can be easily measured from tensile experiments. These formulas are used to calibrate to model parameters. We use the notation of Sec. 3.

A bar of length L and unit cross-section area is subjected to the boundary displacements (3.1), where the mean strain $\varepsilon(t)$ is supposed to be non-negative, as in tensile tests. In this one-dimensional framework, the plastic strain tensor $\boldsymbol{p}$ reduces to the scalar plastic stretching p. The flow rule (4.28) rewrites $\dot{p} = \mathrm{sign}(\sigma_{\mathrm{II}})\dot{\bar{p}}$, with σ_{II} the tensile stress of phase II. Since $\sigma_{\mathrm{II}} \geq 0$ in tensile tests, the plastic strain coincides with the accumulated plastic strain. Thus it satisfies the constrain

$$\dot{p} \geq 0. \tag{4.37}$$

The total internal energy (4.6) simplifies as follows

$$\begin{aligned}\mathcal{W}(u_{\mathrm{I}}, u_{\mathrm{II}}, d, p) = \quad & \int_0^l v_{\mathrm{I}} \left(\frac{1}{2}\mathsf{g}(d)\mathsf{E}_{\mathrm{I}} u_{\mathrm{I}}'^2 + \mathsf{w}_{\mathrm{I}}(d) + \frac{1}{2}\overline{\mathsf{w}}_{\mathrm{I}}\ell_{\mathrm{I}}^2 d'^2 \right) dx + \\ & + \int_0^l v_{\mathrm{II}} \left(\frac{1}{2}\mathsf{E}_{\mathrm{II}}(u_{\mathrm{II}}' - p)^2 + \mathsf{w}_{\mathrm{II}}(p) + \frac{1}{2}\overline{\mathsf{w}}_{\mathrm{II}}\ell_{\mathrm{II}}^2 p'^2 \right) dx + \\ & + \int_0^l \frac{1}{2}\frac{\mathsf{E}_{\mathrm{k}}}{\ell_{\mathrm{k}}^2}(u_{\mathrm{I}} - u_{\mathrm{II}})^2 \, dx,\end{aligned} \tag{4.38}$$

where the three integrals correspond to the energy of phases I and II and to the bond energy. Coefficients E_{I} and E_{II} are the Young's moduli of the two phases. The normal stresses in the two phases, and the exchanged shear force are

$$\sigma_{\mathrm{I}} = \mathsf{g}(d)\mathsf{E}_{\mathrm{I}} u_{\mathrm{I}}', \quad \sigma_{\mathrm{II}} = \mathsf{E}_{\mathrm{II}}(u_{\mathrm{II}}' - p), \quad \tau = \frac{\mathsf{E}_{\mathrm{k}}}{\ell_{\mathrm{k}}^2}(u_{\mathrm{I}} - u_{\mathrm{II}}), \tag{4.39}$$

which are obtained by differentiating the elastic energy densities with respect to strains and the bond energy density with respect to the relative displacement. Non-negativeness of the total energy first variation

$$\delta\mathcal{W}(u_{\mathrm{I}}, u_{\mathrm{II}}, d, p)[\tilde{u}_{\mathrm{I}}, \tilde{u}_{\mathrm{II}}, \tilde{d}, \tilde{p}] \geq 0, \tag{4.40}$$

for any perturbation $(\tilde{u}_{\mathrm{I}}, \tilde{u}_{\mathrm{II}}, \tilde{d}, \tilde{p})$, such that $\tilde{u}_{\mathrm{I}}(0) = \tilde{u}_{\mathrm{II}}(0) = 0$, $\tilde{u}_{\mathrm{I}}(L) = \tilde{u}_{\mathrm{II}}(L) = 0$, $\tilde{d} \geq 0$ and $\tilde{p} \geq 0$, leads to the following relations

$$\begin{aligned} & v_{\mathrm{I}}\sigma_{\mathrm{I}}' - \tau = 0, \quad v_{\mathrm{II}}\sigma_{\mathrm{II}}' + \tau = 0, && \text{equilibrium equations,} \\ & f_{\mathrm{I}}(\sigma_{\mathrm{I}}, d, d'') = -2\mathsf{E}_{\mathrm{I}}\frac{\mathsf{g}'(d)}{\mathsf{g}^2(d)}\sigma_{\mathrm{I}}^2 - \mathsf{w}_{\mathrm{I}}'(d) + \overline{\mathsf{w}}_{\mathrm{I}}\ell_{\mathrm{I}}^2 d'' \leq 0, && \text{damage yield condition,} \\ & f_{\mathrm{II}}(\sigma_{\mathrm{II}}, p, p'') = \sigma_{\mathrm{II}} - \mathsf{w}_{\mathrm{II}}'(p) + \overline{\mathsf{w}}_{\mathrm{II}}\ell_{\mathrm{II}}^2 p'' \leq 0, && \text{plasticity yield condition,} \end{aligned} \tag{4.41}$$

which are the one-dimensional counterparts of equations (4.18), (4.20), and (4.22). The macroscopic balance equations $(4.41)_{1,2}$ are equal to (3.11). To satisfy the variational inequality (4.40), the boundary conditions

$$d'(0) \leq 0,\ d'(L) \geq 0, \qquad p'(0) \leq 0,\ p'(L) \geq 0, \tag{4.42}$$

must also be imposed. Equation (eb) of energy balance specializes as follows

$$\dot{\mathcal{W}}(u_{\mathrm{I}}, u_{\mathrm{II}}, d, p) = (v_{\mathrm{I}}\sigma_{\mathrm{I}} + v_{\mathrm{II}}\sigma_{\mathrm{II}})\,\dot{\varepsilon}, \tag{4.43}$$

from which the consistency conditions descent

$$f_{\mathrm{I}}(\sigma_{\mathrm{I}}, d, d'')\dot{d} = 0, \quad f_{\mathrm{II}}(\sigma_{\mathrm{II}}, \bar{p}, \bar{p}'')\dot{\bar{p}} = 0, \tag{4.44}$$

with the boundary conditions

$$d'(0) = d'(L) = 0, \qquad p'(0) = p'(L) = 0, \tag{4.45}$$

which restrict conditions (4.42) to equalities.

Yield conditions $(4.41)_{3,4}$ can be rewritten in the following form of constraints on stresses

$$\begin{aligned} \sigma_{\mathrm{I}} &\leq \sigma_{\mathrm{f}}(d, d'') := \sqrt{-2\mathsf{E}_{\mathrm{I}}\frac{\mathsf{g}^2(d)}{\mathsf{g}'(d)}\left(\mathsf{w}_{\mathrm{I}}'(d) + \overline{\mathsf{w}}_{\mathrm{I}}\ell_{\mathrm{I}}^2 d''\right)}, \\ \sigma_{\mathrm{II}} &\leq \sigma_{\mathrm{p}}(p, p'') := \mathsf{w}_{\mathrm{II}}'(p) - \overline{\mathsf{w}}_{\mathrm{II}}\ell_{\mathrm{II}}^2 p'', \end{aligned} \tag{4.46}$$

with σ_{f} and σ_{p} the elastic limit stresses of phase I and II, respectively. We define

$$\bar{\sigma}_{\mathrm{f}} := \sigma_{\mathrm{f}}(0,0) = \sqrt{-2\mathsf{E}_{\mathrm{I}}\frac{\mathsf{w}_{\mathrm{I}}'(0)}{\mathsf{g}'(0)}}, \qquad \bar{\sigma}_{\mathrm{p}} := \sigma_{\mathrm{p}}(0,0) = \mathsf{w}_{\mathrm{II}}'(0), \tag{4.47}$$

as the maximum stresses that can be elastically sustained by phase I and phase II, respectively. When the stress $\bar{\sigma}_{\mathrm{f}}$ is reached, a fracture can form, and, when the stress $\bar{\sigma}_{\mathrm{p}}$ is attained, plastic strains can develop. By inverting the above relations, we obtain

$$\frac{\mathsf{w}_{\mathrm{I}}'(0)}{\mathsf{g}'(0)} = -\frac{\bar{\sigma}_{\mathrm{f}}^2}{2\mathsf{E}_{\mathrm{I}}}, \qquad \mathsf{w}_{\mathrm{II}}'(0) = \bar{\sigma}_{\mathrm{p}}, \tag{4.48}$$

which are used in Sec. 4.6 to calibrate parameters of w_{I} and w_{II}. Indeed, quantities on the right-hand sides can be easily estimated from tensile tests.

4.5.1. Limit models for an infinite soft and infinite rigid relative displacement stiffness

The relative displacement stiffness $\mathsf{E}_{\mathrm{k}}/\ell_{\mathrm{k}}^2 =: \mathsf{K}$ plays a key role in the global response of the composite material. Hereafter the limit cases for an infinite soft and infinite rigid relative displacement stiffness are discussed.

Case $\mathsf{K} \to 0$. In this case, the last integral in (4.38) vanishes. Therefore, no interaction exists anymore between the two phases and the global material response corresponds to a plain superposition of the individual responses of the two phases.

Case $\mathsf{K} \to \infty$. This case is more intriguing. In order to keep the total internal energy finite, a rigid relative displacement stiffness forces the displacement fields of the two phases to be the same ($\delta = 0$). As a result, the model depends only on one displacement field, namely $u_{\mathrm{I}} = u_{\mathrm{II}} = u$. The resulting total internal energy becomes

$$\mathcal{W}(u,d,p) = \int_0^L \left(\frac{1}{2} \left(v_{\mathrm{I}}(1-d)^2 \mathsf{E}_{\mathrm{I}} + v_{\mathrm{II}} \mathsf{E}_{\mathrm{II}} \right) \varepsilon^2 - v_{\mathrm{II}} \mathsf{E}_{\mathrm{II}} u' p + \frac{1}{2} v_{\mathrm{II}} \mathsf{E}_{\mathrm{II}} p^2 \right) \mathrm{d}x + \\ + \int_0^L \left(v_{\mathrm{I}} \left(\mathsf{w}_{\mathrm{I}}(d) + \frac{1}{2} \overline{\mathsf{w}}_{\mathrm{I}} \ell_{\mathrm{I}}^2 d'^2 \right) + v_{\mathrm{II}} \left(\mathsf{w}_{\mathrm{II}}(p) + \frac{1}{2} \overline{\mathsf{w}}_{\mathrm{II}} \ell_{\mathrm{II}}^2 p'^2 \right) \right) \mathrm{d}x \quad (4.49)$$

A qualitative homogeneous response, without non-local effects, of this limit model is sketched in Fig. 11. The global response is well represented by a coupled damage-plasticity model where damage degrades only part of the elastic stiffness. The global response has therefore strong analogies with the gradient-damage plasticity models developed and discussed in [60, 35].

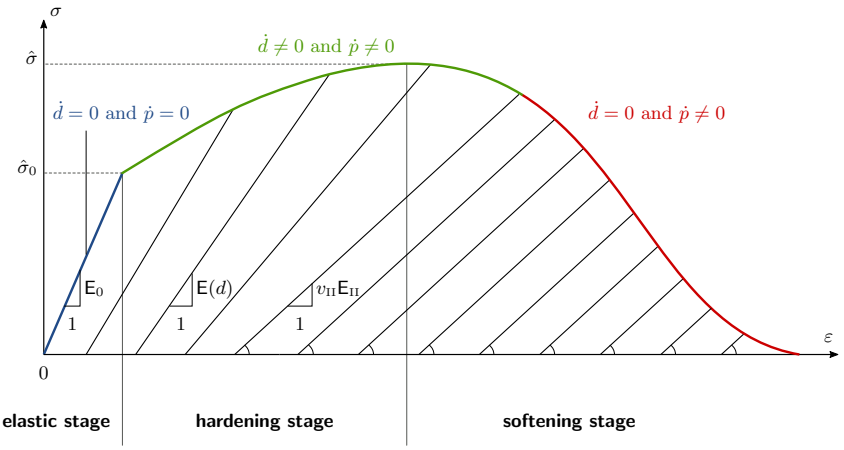

Figure 11: Qualitative homogeneous response of the limit model (4.49). Damage is assumed to stop its evolution after the hardening stage. In the figure $\mathsf{E}_0 = v_{\mathrm{I}}\mathsf{E}_{\mathrm{I}} + v_{\mathrm{II}}\mathsf{E}_{\mathrm{II}}$ and $\mathsf{E}(d) = v_{\mathrm{I}}(1-d)^2\mathsf{E}_{\mathrm{I}} + v_{\mathrm{II}}\mathsf{E}_{\mathrm{II}}$.

4.6. Constitutive assumptions and parameters calibration

In this section, specific functions are assigned to elastic, damage and plastic energy densities, and criteria are proposed to calibrate the constitutive parameters of the model. The specific constitutive assumptions are suggested by the peculiar mechanical response of UHPFRC described in Sec. 2.1. Here, UHPFRC is chosen as an example, but the model is quite general, and it can be applied to different composites. Obviously, different shapes of the energy densities must be chosen in order to properly describe the specific mechanical behavior of the considered composite.

Since we suppose that fibers are homogeneously distributed and randomly oriented within an isotropic matrix, we specialize the elastic tensors $\mathbb{C}_{\mathrm{I}}$ and $\mathbb{C}_{\mathrm{II}}$ to the case of isotropic materials

$$\mathbb{C}_i = \frac{\mathsf{E}_i}{1+\nu_i} \left(\mathbb{I} + \frac{\nu_i}{1-2\nu_i} \mathbf{I} \otimes \mathbf{I} \right), \quad i = \mathrm{I}, \mathrm{II}, \quad (4.50)$$

with $\mathbb{I}$ and $\mathbf{I}$ the fourth and second order identity tensors, E_i the Young's modulus, and ν_i the Poisson's ratio.

For the degradation function g and the damage energy density, we assume

$$\mathsf{g}(d) = (1-d)^2, \quad \mathsf{w}_{\mathrm{I}}(d) = \overline{\mathsf{w}}_{\mathrm{I}} d, \quad (4.51)$$

where the expression of g is that usually considered in phase-field models [25], and the linear dependence of $\mathsf{w}_{\rm I}$ on d allows to account for an initial undamaged elastic stretching. To calibrate parameter $\overline{\mathsf{w}}_{\rm I}$, we use equation $(4.48)_1$, which specializes as follows

$$\overline{\mathsf{w}}_{\rm I} = \frac{\bar{\sigma}_{\rm f}^{\,2}}{\mathsf{E}_{\rm I}}, \tag{4.52}$$

where the quantities on the right-hand side are usually known (they can be easily be estimated from tensile tests). If the composite stress-strain curve is available, like the curve of Fig. 1b, $\bar{\sigma}_{\rm f}$ can be estimate from $\hat{\sigma}_0$ by the formula

$$\bar{\sigma}_{\rm f} = \frac{\mathsf{E}_{\rm I}}{v_{\rm I}\mathsf{E}_{\rm I} + v_{\rm II}\mathsf{E}_{\rm II}}\hat{\sigma}_0. \tag{4.53}$$

The internal length $\ell_{\rm I}$ is related to the fracture process zone size $\ell_{\rm f}$ through the formula

$$\ell_{\rm I} = \frac{\ell_{\rm f}}{2\sqrt{2}}, \tag{4.54}$$

obtained in [25] by solving $(4.41)_2$. In case of matrices made of aggregates of different sizes (like concrete) the process zone size is about 2-3 times the size of the largest aggregates.

To properly assign the shape of the plastic energy density $\mathsf{w}_{\rm II}$, we recall some features of the UHPFRC response described in Sec. 2.1. Plastic strains develop in the stress-hardening stage of progressive micro-cracking, and, at the end of this phase, the mean accumulated plastic strain is the permanent strain $\hat{\varepsilon}_p$ reported in Fig. 1b, which is determined by unloading the specimen when the tensile process has reached the hardening-to-softening transition point. In the softening stage, plastic strains accumulates around a single crack, which develops into a macro-crack.

Since a convex plastic energy promotes the evolution of diffused plastic strains in regime of stress-hardening, and, on the contrary, a concave energy produces plastic strain localization in stress-softening regime [41, 43, 33], we assume a convex-concave plastic energy density, in order to reproduce the two consecutive plastic stages of diffused and localized strains observed in experiments. A simple choice, fulfilling the above requirements, is the following piecewise quadratic expression

$$\mathsf{w}_{\rm II}(\bar{p}) = \begin{cases} \frac{1}{2}\mathsf{h}_{\rm p}\bar{p}^2 + \bar{\sigma}_{\rm p}\bar{p}, & \text{if } 0 < \bar{p} \le \hat{p}, \\ -\frac{1}{2}\mathsf{s}_{\rm p}\,(\bar{p}-\hat{p})^2 + \hat{\sigma}_{\rm p}\,(\bar{p}-\hat{p}) + \frac{1}{2}\mathsf{h}_{\rm p}\hat{p}^2 + \bar{\sigma}_{\rm p}\hat{p}, & \text{if } \bar{p} > \hat{p}, \end{cases} \tag{4.55}$$

whose derivative is

$$\mathsf{w}'_{\rm II}(\bar{p}) = \begin{cases} \mathsf{h}_{\rm p}\bar{p} + \bar{\sigma}_{\rm p}, & \text{if } 0 < \bar{p} \le \hat{p}, \\ -\mathsf{s}_{\rm p}\,(\bar{p}-\hat{p}) + \hat{\sigma}_{\rm p}, & \text{if } \bar{p} > \hat{p}, \end{cases} \tag{4.56}$$

which is very similar to the yield stress law (3.5) of Sec. 3. Graphs of (4.55) and (4.56) are plotted in Fig. 12. Coefficients to be assigned in (4.55) are the activation stress $\bar{\sigma}_{\rm p}$, the peak stress $\hat{\sigma}_{\rm p}$, the corresponding strain $\hat{p}$, and the softening modulus $\mathsf{s}_{\rm p}$. The hardening modulus is $\mathsf{h}_{\rm p} = (\hat{\sigma}_{\rm p} - \bar{\sigma}_{\rm p})/\hat{p}$, and it depends on the listed quantities.

The stress $\bar{\sigma}_{\rm p}$ must satisfy conditions (3.38), which ensure plasticity development after crack opening, as observed in experiments. The peak stress $\hat{\sigma}_{\rm p}$ is equal to the maximum stress $\hat{\sigma}$ registered in a tensile experiments (see Fig. 1b). The corresponding plastic strain $\hat{p}$ is related to the mean accumulated plastic strain $\hat{\varepsilon}_{\rm p}$ of Fig. 1b. At the end of the hardening stage, $\bar{p}$ is not homogeneous, and the maximum values attained in correspondence of cracks should be $\hat{p}$. Since $\hat{p} = \max \bar{p}(x) > \text{mean}\, \bar{p}(x) = \hat{\varepsilon}_{\rm p}$, a value of $\hat{p}$ larger than $\hat{\varepsilon}_{\rm p}$ should be assigned.

The remaining quantities to be characterized are the softening coefficient s_p, and the coefficients $\overline{\mathsf{w}}_\mathrm{II}$ and ℓ_II of the non-local plastic energy. The internal length ℓ_II is the size of the macro-crack process zone, and it should not exceed the minimum micro-crack spacing ℓ_k, introduced in Sec. 3.3. To calibrate s_p and $\overline{\mathsf{w}}_\mathrm{II}$, we use formulas (39) and $(41)_2$ of [43], which express the size ℓ_II of the localization zone and the negative slope E_s of the softening branch (see Fig. 1b) as functions of L, E_II, s_p and $\overline{\mathsf{w}}_\mathrm{II}\ell_\mathrm{II}^2$. Their expressions, adapted to the present notation, are

$$\ell_\mathrm{II} = 2\pi\sqrt{\frac{\overline{\mathsf{w}}_\mathrm{II}\ell_\mathrm{II}^2}{\mathsf{s}_\mathrm{p}}}, \qquad \mathsf{E}_\mathrm{s} = -\mathsf{s}_\mathrm{p}\left(\frac{2\pi}{L}\sqrt{\frac{\overline{\mathsf{w}}_\mathrm{II}\ell_\mathrm{II}^2}{\mathsf{s}_\mathrm{p}}} - \frac{\mathsf{s}_\mathrm{p}}{\mathsf{E}_\mathrm{II}}\right)^{-1}, \tag{4.57}$$

from which

$$\mathsf{s}_\mathrm{p} = -\mathsf{E}_\mathrm{s}\frac{\ell_\mathrm{II}}{L}\left(1 - \frac{\mathsf{E}_\mathrm{s}}{\mathsf{E}_\mathrm{II}}\right)^{-1}, \qquad \overline{\mathsf{w}}_\mathrm{II} = \frac{\mathsf{s}_\mathrm{p}}{4\pi^2}, \tag{4.58}$$

which are used to calibrate s_p and $\overline{\mathsf{w}}_\mathrm{II}$, since terms on the right-hand sides are known.

Finally, parameters E_k and ℓ_k of the bond energy are fixed according to the results of Sec. 3.3: ℓ_k is the spacing between adjacent micro-cracks, easily observable in tensile tests, and modulus E_k is given by formula (3.25).

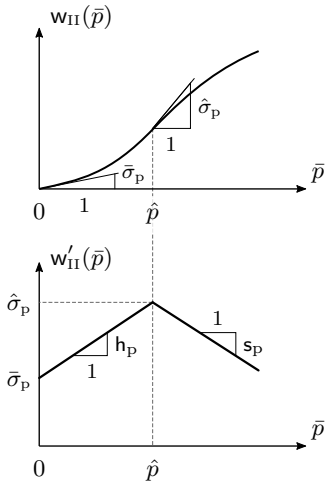

Figure 12: Graphs of functions $\mathsf{w}_\mathrm{II}(\bar{p})$ and $\mathsf{w}'_\mathrm{II}(\bar{p})$.

5. Numerical simulations

In this section, numerical results are presented. The evolution scheme described in Sec. 4.4 is numerically implemented in a finite element code, developed within Matlab® environment. In the next Sec. 5.1, experimental results of [8] are reproduced by implementing the one-dimensional model of Sec. 4.5, and two-dimensional tests are proposed in Sec. 5.2. In all the cases, values of the model parameters are taken from [8]. Among the many experimental results proposed in [8], where different kinds of fibers with different volume fractions are tested, we consider the case of straight fibers with volume fraction equal to 2.5%, labeled U-S-2.5 in [8]. For this mixture, values are listed in the following.

- *Phases volume fractions.* $v_\mathrm{I} = 0.975$, $v_\mathrm{II} = 0.025$.
- *Young's moduli.* $\mathsf{E}_\mathrm{I} = 57000\,\mathrm{MPa}$, $\mathsf{E}_\mathrm{II} = 210000\,\mathrm{MPa}$, corresponding to ultra-high performance concrete and steel, respectively.

- *Internal lengths.* $\ell_{\rm k} = 5\,$mm, corresponding to the micro-crack interspacing observed in experiments; $\ell_{\rm f} = 1\,$mm, which is slightly bigger than the maximum size of concrete aggregates equal to 0.8 mm; $\ell_{\rm II} = 5\,$mm which is about 1.5 times the fiber length of 3 mm, as suggested in [61].

- *Peak stress of phase* I. $\sigma_{\rm f} = 11.25\,$MPa, obtained from (4.53), where the peak stress $\hat\sigma_0 = 12\,$MPa is taken from [8], Table 7.

- *Parameters of the plastic energy of phase* II. $\bar\sigma_{\rm p} = 5\sigma_{\rm f} = 56.25\,$MPa, which belong to the values range defined by inequalities (3.38); $\hat\sigma_{\rm p} = 660\,$MPa, taken from [8], Table 7; $\hat p = 2.8\cdot 10^{-3}$, which is slightly larger than $\hat\varepsilon_{\rm p} \simeq 2.5\cdot 10^{-3}$, value taken from the stress-strain curve of Fig. 9(c) of [8]; $\mathsf{E}_{\rm s} = \mathsf{E}_{\rm II}/2$, which is the slope of the softening branch, and, from $(4.58)_1$, $\mathsf{s}_{\rm p} = 2.92\cdot 10^4\,$MPa.

- *Non-local plastic coefficient of phase* II. From $(4.58)_2$, $\overline{\mathsf{w}}_{\rm II} = 739\,$MPa.

- *Relative stiffness modulus.* $\mathsf{E}_{\rm k} = 18700\,$MPa, estimated from (3.25).

In the next simulations, the peak stress $\sigma_{\rm f}$ of phase I has been perturbed through a random function of amplitude 0.5%, which reflects material inhomogeneity. In simulations, this perturbation reduces the possibility of simultaneous opening of multiple cracks, favoring the formation of single cracks at a time.

5.1. One-dimensional tensile test

We consider a bar of length $L = 76\,$mm, which is the distance of extensimeter's blades used in [8] to measure specimens stretching. The bar is discretized into 380 finite elements of size 0.2 mm. Within each element, displacements $u_{\rm I}$ and $u_{\rm II}$, and damage d are approximated by quadratic shape functions, depending on three nodal variables defined at the element ending and mid nodes. Plastic strain field p is approximated by linear shape functions, with nodal values defined at the element endpoints.

The stress-strain curve resulting from the simulation is plotted in Fig. 13 (black line), and it is compared with the piecewise linear curve (gray line) obtained in [8] through a regularization procedure of the experimental curves. The numerical curve captures the three stages of the evolution: the initial elastic phase, the sawtooth-shaped branch of multi- micro-cracking, with stress drops corresponding to crack openings, and the final stress-softening phase of macro-crack coalescing.

In Fig. 13, unloading branches inform on the amount of damage and plastic strain that accumulate in the bar during the tensile test. The slope of the unloading branches is related to the amount of damage. Since the slope only reduces in the stress-hardening phase, maintaining constant in the next stress-softening stage, damage cumulates only in the intermediate phase of matrix cracking. The permanent strain, given by the intersection of the unloading curve with the strain axis, is an estimate of the accumulated plastic strain. The permanent strain increases both in the hardening and in the softening phase. In the stress-hardening phase, plastic strains develop thereby matrix cracks, diffusing in the whole bar, while, in the stress-softening phase, plasticity localizes around a single pre-existing crack, developing into a macro-crack. These results are in agreement with those given by the discrete analytical model of Sec. 3.6.

The process of matrix cracking is described in Fig. 14, where profiles of damage d are plotted at different values of ε. At each crack, damage localizes in a zones of size $\ell_{\rm I} = 1\,$mm. Cracks progressively distribute in the whole bar, gradually reducing the distance between adjacent fractures. In agreement with the experimental observation, the minimum spacing at the end of

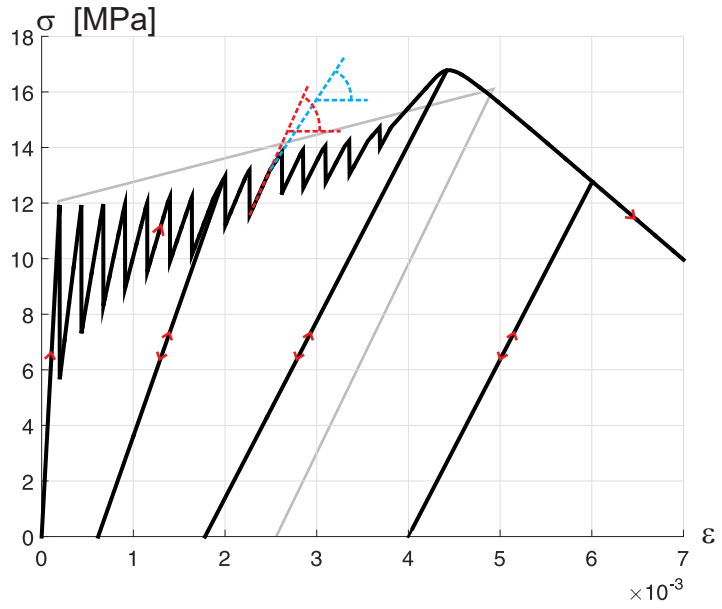

Figure 13: 1D simulation. Numerical stress-strain curve (black line) compared to experimental curve (gray line), taken from figure 8(c) in [8].

the process is about 5 mm, which is, as expected, equal to the internal length ℓ_k assigned in the simulation.

Profiles of displacements u_I and u_{II} and plastic strain p are drawn in Figs. 15 and 16, respectively, for different values of the applied deformation ε. Although displacements are always continuous, u_I steeply increases in correspondence of damage, miming the displacement jump associated to fracture. Displacement u_{II} has a more regular profile, with slope growth nearby cracks. While in the stress-hardening phase, displacement jumps are practically equal in each crack, in the stress-softening stage, displacement grows only in one crack, where plastic strains localize (see bottom-right pictures of Figs. 15 and 16). The plastic strain profiles of Fig. 16 exhibit peak values at crack points. During the micro-cracking stage, the peak value corresponding to the new formed crack is slightly smaller than the peak values of the pre-existing cracks. In the evolution process that follows each crack opening, plastic strain initially grows around the new formed crack, and, when the value of the pre-existing peaks is reached, plastic strains start to increase in the whole bar again. These two phases correspond to the two different slopes exhibited by the response curve within two consecutive stress drops (in Fig. 13, the two slopes are highlighted within one curve tooth). These two evolution steps are imposed as a modeling assumption in the analytical formulation of Sec. 3.5, according to which, between two consecutive crack openings, a single hinge is active in the first stage, and, all hinges actively evolve in the second stage.

In Fig. 17, snapshots of p, σ_I and σ_{II} are plotted at four different values of ε belonging to the evolution stage that leads to the opening of the fourth crack. At $\varepsilon = 0.68$, the third crack has just formed on the left side of the specimens. At the points where fractures have formed, σ_I nullifies and σ_{II} attains the maximum values. Increasing ε, stresses grows, until σ_I reaches the peak stress $\bar{\sigma}_f$ (red line in Fig. 17b) at about $x = 28$ mm, where a new crack forms. The opening of the new fracture produces a stress drop in the whole bar.

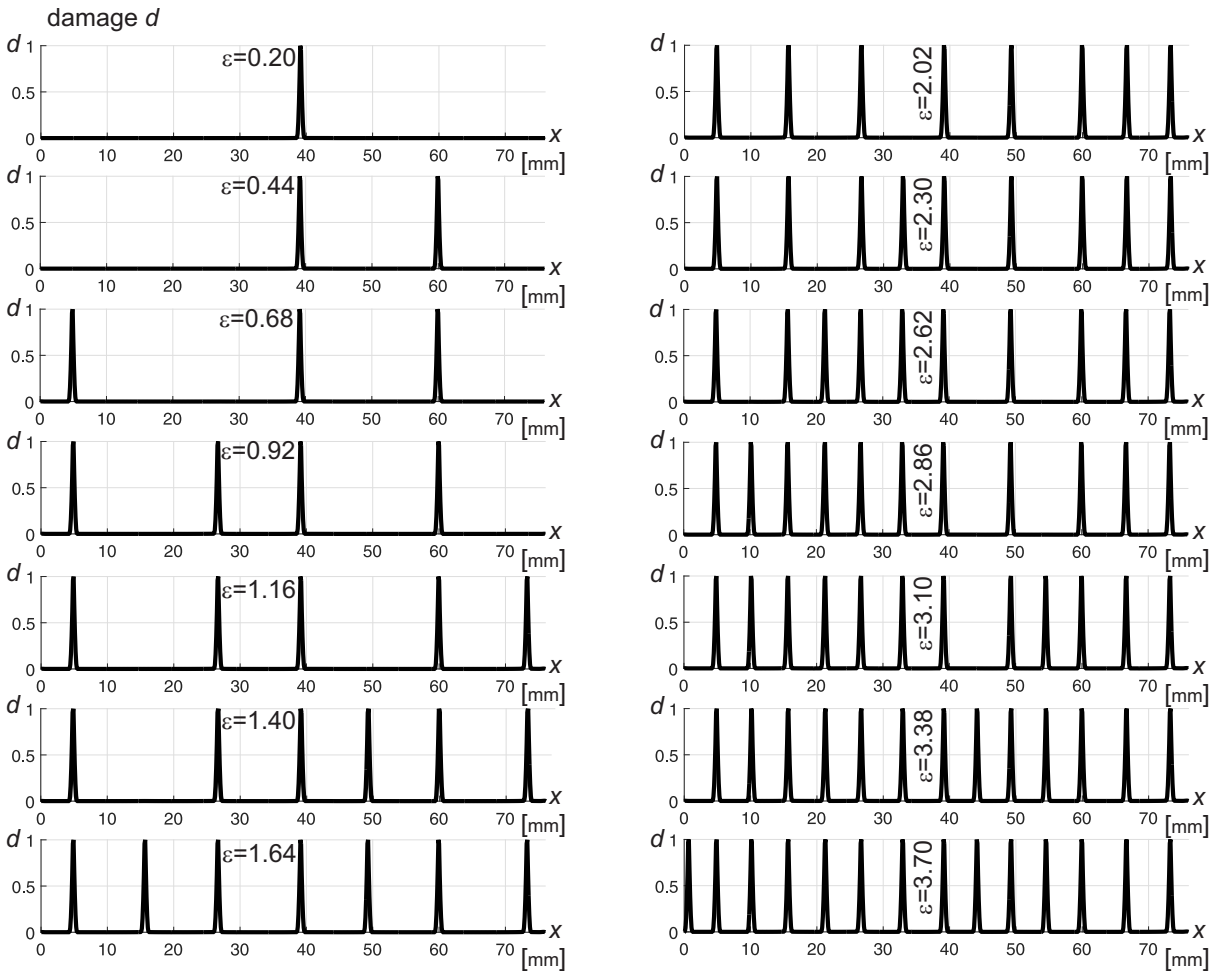

Figure 14: 1D simulation. Profiles of damage d at different values of the imposed deformation ε ($\times 10^{-3}$).

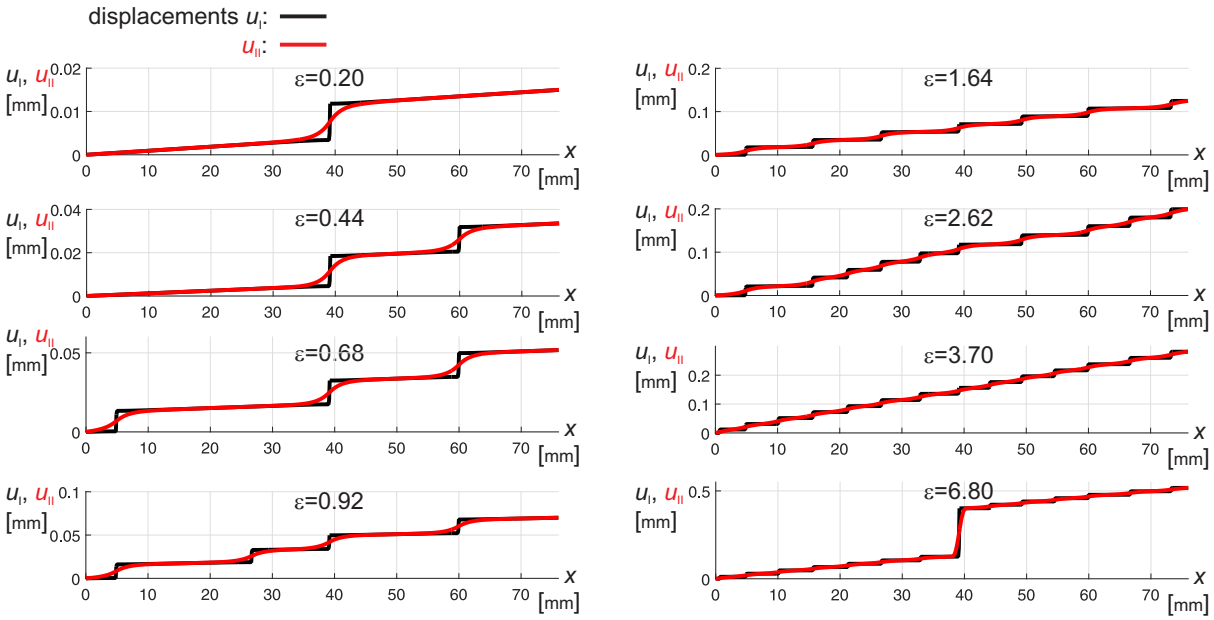

Figure 15: 1D simulation. Profiles of displacements u_{I} and u_{II} at different values of the imposed deformation ε ($\times 10^{-3}$).

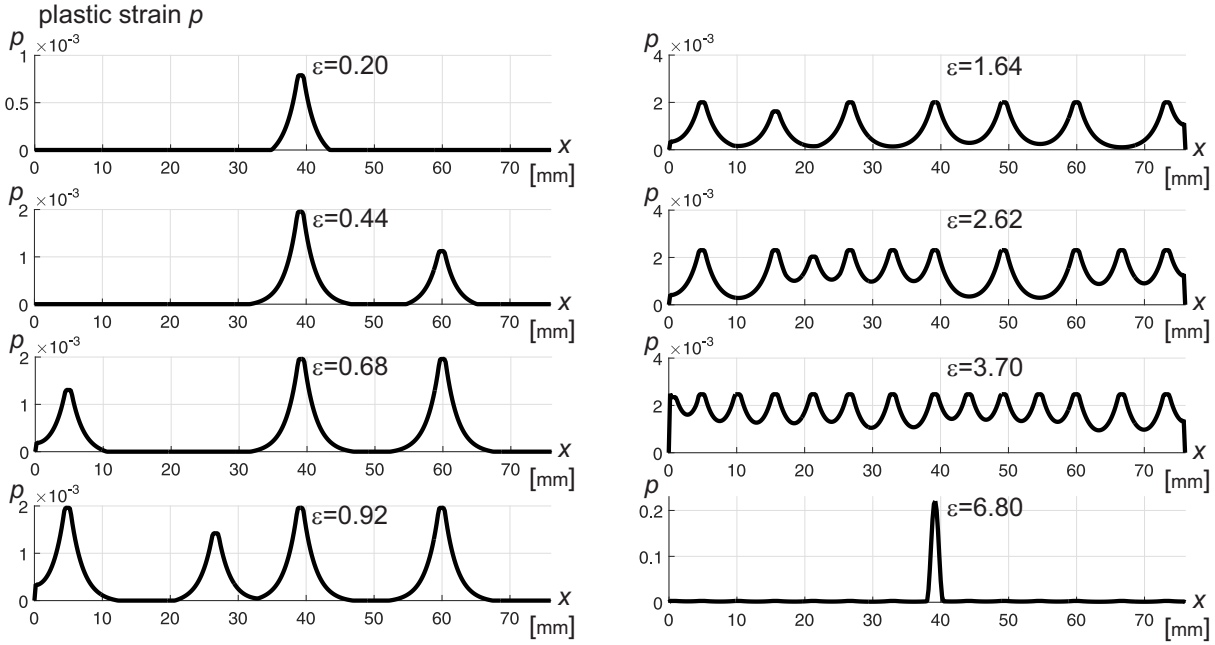

Figure 16: 1D simulation. Profiles of plastic strain p at different values of the imposed deformation ε ($\times 10^{-3}$).

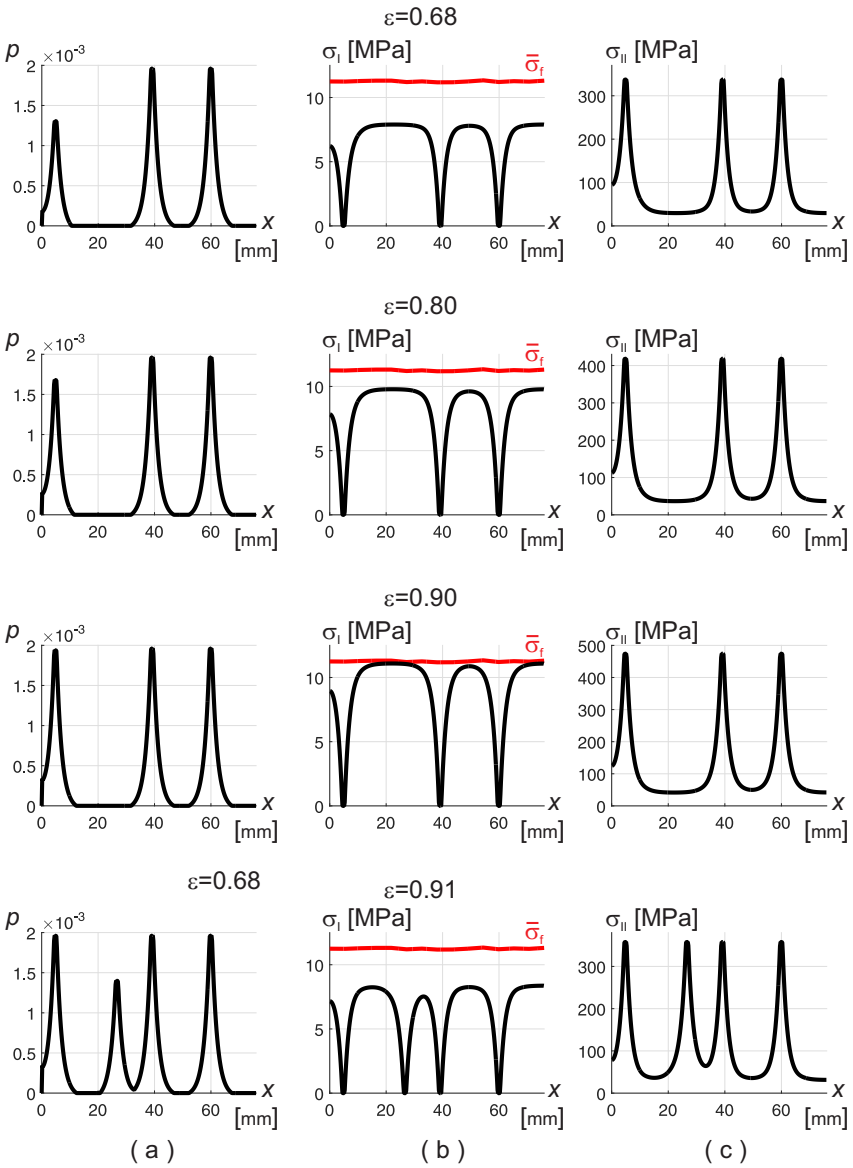

Figure 17: 1D simulation. Fields p (a), σ_{I} (b), and σ_{II} (c) at different values of ε ($\times 10^{-3}$) in the evolution stage from three to four cracks.

5.2. Two-dimensional simulations

In this section, results of two-dimensional simulations are proposed. A tensile test on a dog-bone specimen, and a three point bending test are simulated under the hypothesis of plane stress state. The geometrical schemes of the two simulations are sketched in Fig. 18. In both the cases, domains are discretized by unstructured meshes made of triangular elements. In the tensile test, the specimen response is supposed to be symmetric with respect to the axis y, and, thus, only the right half part of the body is considered. This domain reduction considerably reduces the computational cost.

Six nodal points (triangle vertices and edges midpoints) are considered for each triangular element to approximate displacements $\boldsymbol{u}_{\mathrm{I}}$ and $\boldsymbol{u}_{\mathrm{II}}$, and damage d through quadratic shape functions. Three nodes (triangle vertices) are used to approximate the cumulated plastic strain $\bar{p}$ by linear functions. In Fig. 18b details of the triangular mesh and the nodal points are shown. The maximum edge side of the finite elements is 0.6 mm, which is sufficiently smaller than the internal length $\ell_{\mathrm{I}} = 1\,\mathrm{mm}$. The half dog-bone specimen and the rectangular domain for the bending test are discretized with 2231 elements (4648 nodes), and 5434 (11087 nodes), respectively.

In the numerical code, the degradation function $(4.51)_1$ has been modified as follows

$$\mathrm{g}(d) = (1 - cd)^2, \quad \text{with } c = \begin{cases} 0, & \text{if } \operatorname{div} \boldsymbol{u}_{\mathrm{I}} < 0, \\ 1, & \text{if } \operatorname{div} \boldsymbol{u}_{\mathrm{I}} \geq 0, \end{cases} \tag{5.1}$$

in order to avoid fracture under compressive deformation states ($\operatorname{div} \boldsymbol{u}_{\mathrm{I}} < 0$).

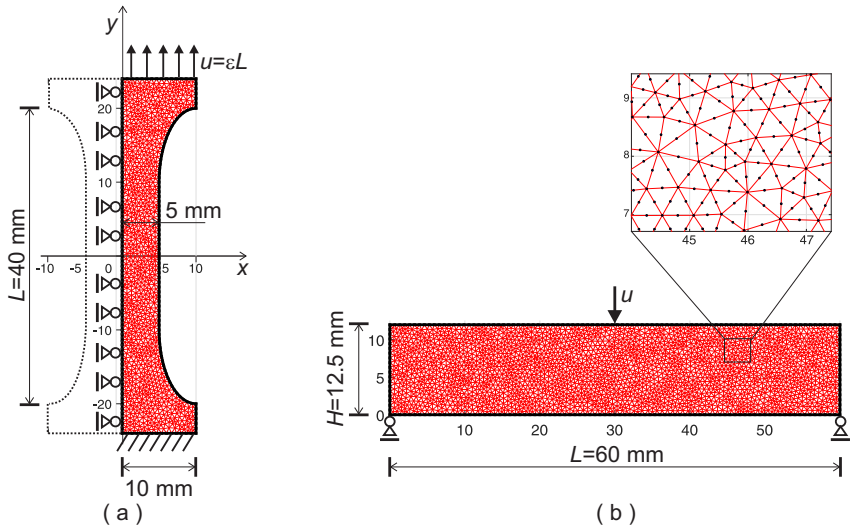

Figure 18: 2D simulations. Geometry, boundary conditions and finite element mesh of specimens for tensile test (a) and three-points bending test (b).

5.2.1. Tensile test on a dog-bone specimen

The stress-strain curve resulting from the tensile test simulation is plotted in Fig. 19. The three branches that characterize the different stages of the evolution can be clearly distinguished. The initial linear elastic branch is followed by the sawtooth branch, associated to matrix cracking. In this latter phase, fractures progressively form within the specimen, according to the sequence of snapshots reported in Fig. 20, where the damage field d is plotted at different values of ε. The first and second cracks open at the extremities of the thinner central part of the sample. This situation is often observed in experiments, because the stress flux through the

specimen shrinkages is not homogeneous, and more vulnerable zones of stress concentration form therein. The third crack opens in the middle cross-section, and, it branches into two fractures. The next fractures distribute in the rest of the sample, and the final spacing between adjacent cracks is about 5 mm, in agreement with the one-dimensional tensile simulation. The irregular profiles of cracks, which present kinks and branches, are mainly due to the random perturbation applied to σ_{f}, which produces material inhomogeneity. In general, it was noticed that the crack evolution predicted by the model is also quite sensitive to geometrical inhomogeneities due to mesh distribution and to time discretization. Although these factors do not change the overall evolution, however they can influence the trajectories of certain cracks.

The evolution of the cumulated plastic strain $\bar{p}$ is described in Fig. 21. In the micro-cracking stage, the plastic strain $\bar{p}$ cumulates nearby the cracks. The stress-hardening phase of micro-cracking terminates when $\bar{p}$ attains the peak strain $\hat{p}$, which, in this simulation, is first reached in correspondence of the crack in the middle cross-section. In the next stress-softening stage, $\bar{p}$ localizes around the central cross-section, as shown by the plastic strain fields of Fig. 21 at $\varepsilon = 4.6 \cdot 10^{-3}$ and $\varepsilon = 5.5 \cdot 10^{-3}$. In that cross-section, the pre-existing matrix crack evolves into a macro-crack. Finally, Fig. 22 reports profiles of the vertical displacements $u_{\mathrm{I}} = \boldsymbol{u}_{\mathrm{I}} \cdot \mathbf{e}_y$ and $u_{\mathrm{II}} = \boldsymbol{u}_{\mathrm{II}} \cdot \mathbf{e}_y$, with $\mathbf{e}_y$ the vertical unit vector, along the axis y, at different steps of the evolution. Profiles are very similar to those of Fig. 15, resulting from the one-dimensional test. The displacement jump generated by plastic strain localization can be clearly observed in the profiles at $\varepsilon = 5.5 \cdot 10^{-3}$.

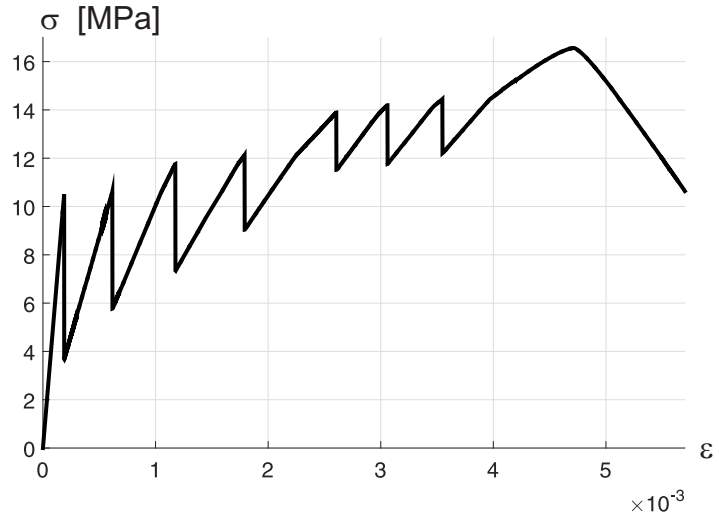

Figure 19: 2D tensile test. Stress-strain curve of tensile test on dog-bone specimen.

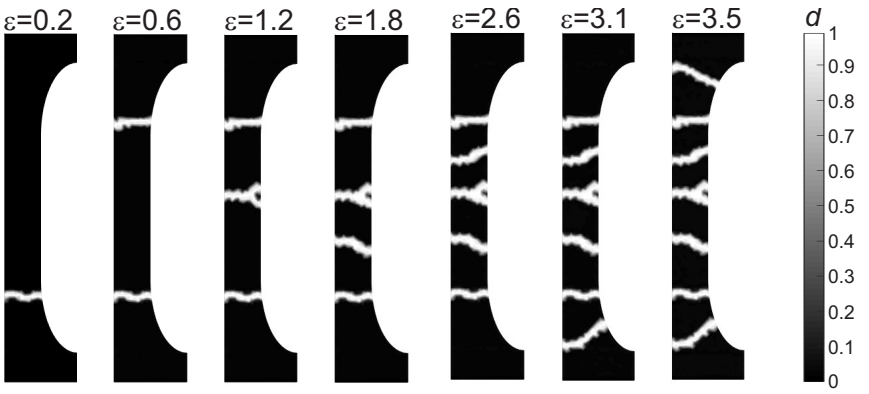

Figure 20: 2D tensile test. Damage field d at different values of the imposed deformation ε ($\times 10^{-3}$).

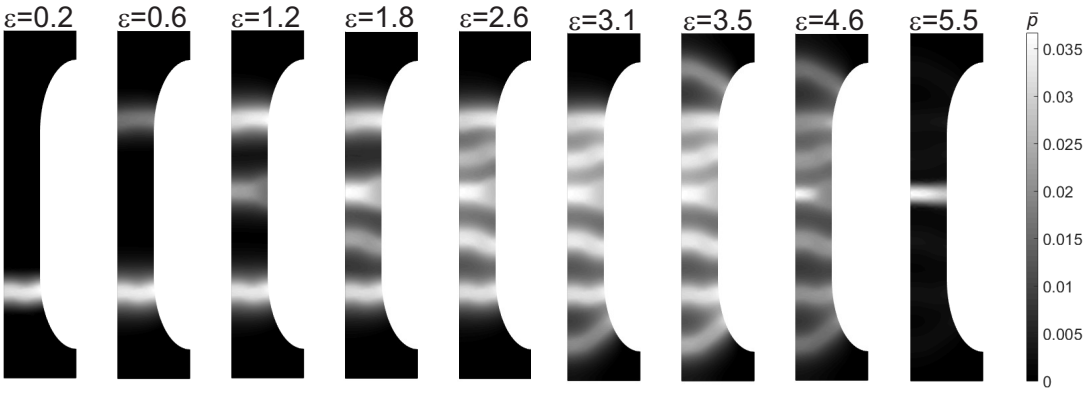

Figure 21: 2D tensile test. Cumulated plastic strain field $\bar{p}$ at different values of the imposed deformation ε ($\times 10^{-3}$).

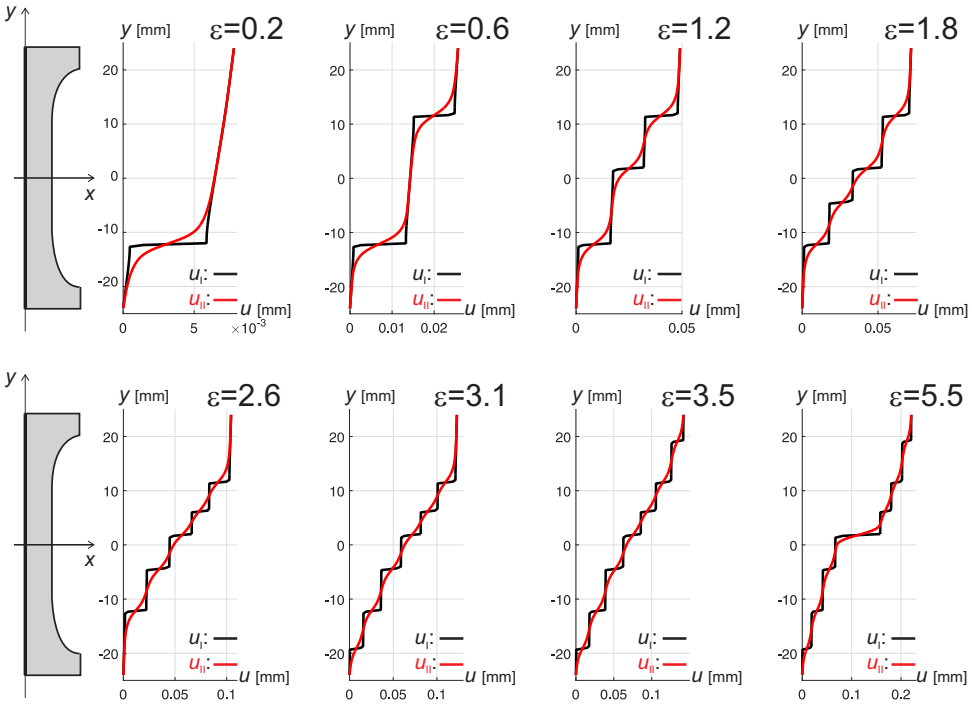

Figure 22: 2D tensile test. Vertical displacements u_{I} and u_{II} along the axis y at different values of the imposed deformation ε ($\times 10^{-3}$).

5.2.2. Three-points bending test

The simulation of a three-points bending test gives the response curve of Fig. 23, where the reactive force f at the specimen supports is plotted versus the imposed displacement u. Also in this case, the curve decomposes into a linear elastic branch, a stress-hardening sawtooth branch, and a softening branch. Stress drops correspond to the opening of cracks in the bottom central part of the specimen, as shown by the damage contours of Fig. 24. The first crack opens in the bottom half-span point of the beam, where the maximum tensile stress is attained, and it propagates upward. The next fractures form in the central part of the domain. They activate at the bottom side of the beam, and propagate upward, bending toward the upside midpoint, where displacement u is applied, and resulting in curved trajectories. The fracture patterning accurately reproduces the cracking scenarios usually observed in experiments, where fractures are basically orthogonal to the isostatic lines of maximum tension. Mainly, at late stages of the evolution, cracks undergo phenomena of branching and merging, which complicate the fracture patterning, as shown by the damage map at $u = 0.29\,\text{mm}$.

The evolution of the cumulated plastic strain associated to the cracking process is described in Fig. 25. The plastic strain grows in the bottom part of the specimen, in correspondence of the cracks. In the last stage of stress-softening, $\bar{p}$ localizes nearby the central crack, and, therein, the macro-crack develops.

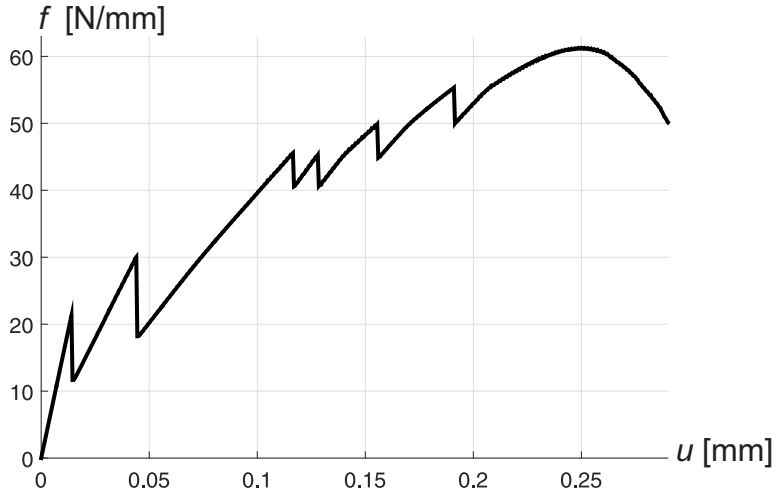

Figure 23: 2D bending test. Force-displacement curve of three-point bending test.

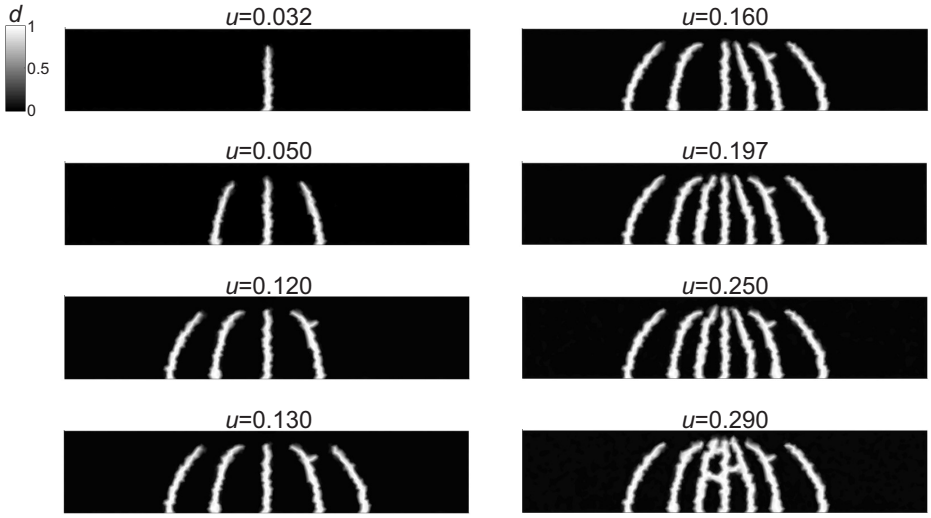

Figure 24: 2D bending test. Damage field d at different values of the imposed displacement u [mm].

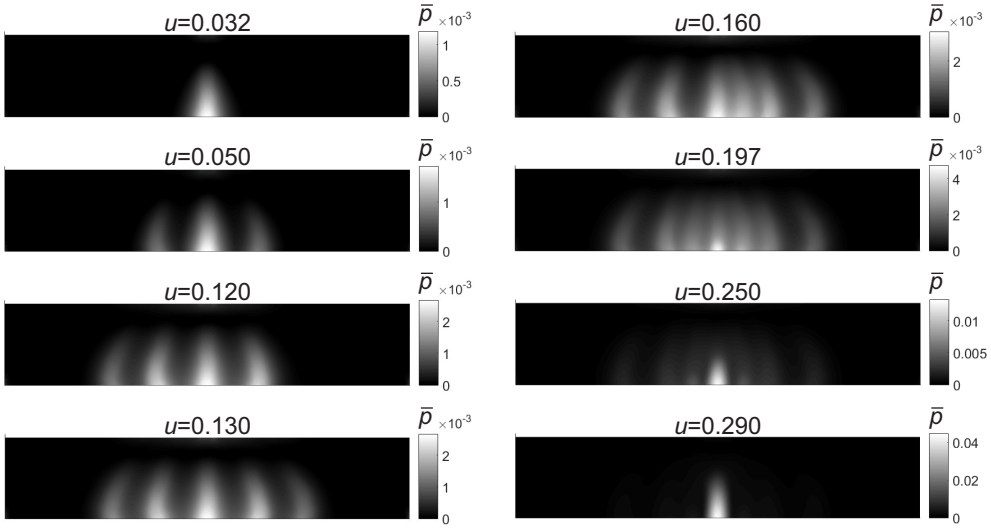

Figure 25: 2D bending test. Cumulated plastic strain field $\bar{p}$ at different values of the imposed displacement u [mm].

6. Conclusions and Perspectives

A novel variational model for the description of the tensile dominated failure in short fiber-reinforced composites has been proposed. The composite is represented as a mixture of two phases linked by elastic springs. One phase represents a brittle matrix, modeled by a non-local phase-field model, whereas the other phase represents dispersed ductile fibres, modeled by a non-local plasticity model. Equilibrium equations and evolution laws for the internal state variables are variationally deduced, once the energy functional has been assigned. The model has been numerically implemented in a finite element code and the evolution problem has been solved by an incremental energy minimization algorithm.

Analytical solutions of a simplified model and numerical results have shown the capability of the model in capturing the main features of the failure process experienced by UHPFRC, taken as an example of short fiber-reinforced composites. The model has been proved to properly describe the progressive formation of multiple micro-cracks within the matrix, and the subsequent macro-fracture opening, properly interpreting the stress bridging action of fibers. It has been

found that the whole tensile failure process is governed by the three different internal lengths, i.e., ℓ_{I}, ℓ_{II} and ℓ_{k}, which are incorporated into the energy (4.6). The strict dependence of the crack patterning on these characteristic lengths is shown in Fig. 26, where the phase-field localization width in the brittle phase, the plastic-strain localization width in the ductile phase, and the crack spacing length are highlighted. Also the dissipation mechanisms found in experiments have been captured by the model which combines damage and plasticity dissipations.

The calibration of constitutive parameters has been discussed, providing simple formulas for their identification from data which can be directly measured from tensile experiments. Due to the great flexibility of the variational formulation, the developed model can be tuned for the description of the mechanical response of many other fibre-reinforced composite materials, by just changing the values of the constitutive parameters.

In this work, the attention has been focused on tensile dominated behaviours. In shear and compression, different phenomena may be expected and this model can represent a valid starting point for further enrichments. Furthermore, a key aspect that deserve a more careful analysis in the future is the coupling elastic term by considering, for instance, the effect of non linear and anisotropic laws [62], possibly derived from micromechanical models of crack bridging [53, 63].

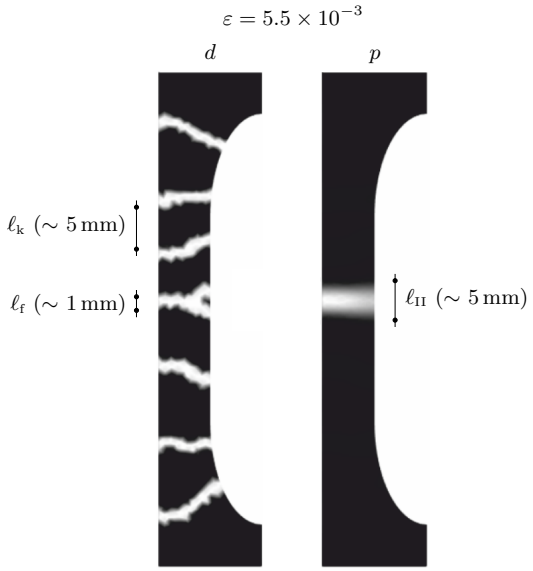

Figure 26: Damage and plastic strains snapshots at failure of the tensile test of Sec. 5.2.1, where the three characteristic lengths (phase-field localization width $\ell_{\mathrm{f}} = 2\sqrt{2}\ell_{\mathrm{I}}$, plastic-strain localization width ℓ_{II}, and micro-crack spacing length ℓ_{k}) are highlighted.

References

[1] S. Abrate, The Mechanics of Short Fiber-Reinforced Composites: A Review, Rubber Chemistry and Technology 59 (3) (1986) 384–404.

[2] P. J. Herrera-Franco, A. Valadez-González, A study of the mechanical properties of short natural-fiber reinforced composites, Composites Part B: Engineering 36 (8) (2005) 597–608.

[3] D. N. Saheb, J. P. Jog, Natural fiber polymer composites: A review, Advances in Polymer Technology 18 (4) (1999) 351–363.

[4] S.-Y. Fu, B. Lauke, Y.-W. Mai, Science and engineering of short fibre reinforced polymer composites., Woodhead, 2019.

[5] A. Bentur, S. Mindess, Fibre Reinforced Cementitious Composites, 2nd Edition, CRC Press, 2007.

[6] S. H. Park, D. J. Kim, G. S. Ryu, K. T. Koh, Tensile behavior of ultra high performance hybrid fiber reinforced concrete, Cement and Concrete Composites 34 (2) (2012) 172–184.

[7] D. L. Nguyen, G. S. Ryu, K. T. Koh, D. J. Kim, Size and geometry dependent tensile behavior of ultra-high-performance fiber-reinforced concrete, Composites Part B: Engineering 58 (2014) 279–292.

[8] K. Wille, S. El-Tawil, A. E. Naaman, Properties of strain hardening ultra high performance fiber reinforced concrete (UHP-FRC) under direct tensile loading, Cement and Concrete Composites 48 (2014) 53–66.

[9] R. Yu, P. Spiesz, H. J. H. Brouwers, Mix design and properties assessment of Ultra-High Performance Fibre Reinforced Concrete (UHPFRC), Cement and Concrete Research 56 (2014) 29–39.

[10] D.-Y. Yoo, N. Banthia, Mechanical properties of ultra-high-performance fiber-reinforced concrete: A review, Cement and Concrete Composites 73 (2016) 267–280.

[11] K. Pham, J.-J. Marigo, C. Maurini, The issues of the uniqueness and the stability of the homogeneous response in uniaxial tests with gradient damage models, Journal of the Mechanics and Physics of Solids 59 (6) (2011) 1163–1190.

[12] E. Baioni, R. Alessi, V. Corinaldesi, G. Lancioni, R. Rizzini, Feasibility Study of a Table Prototype Made of High-Performance Fiber-Reinforced Concrete, Technologies 5 (3) (2017).

[13] M. Jalalvand, G. Czél, M. R. Wisnom, Damage analysis of pseudo-ductile thin-ply UD hybrid composites – A new analytical method, Composites Part A: Applied Science and Manufacturing 69 (2015) 83–93.

[14] Y. Leterrier, D. Pellaton, D. Mendels, R. Glauser, J. Andersons, J.-A. E. Manson, Biaxial fragmentation of thin silicon oxide coatings on poly (ethylene terephthalate), Journal of Materials Science 36 (2001) 2213–2225.

[15] V. Lazarus, Fracture spacing in tensile brittle layers adhering to a rigid substrate, EPL (Europhysics Letters) 117 (2) (2017) 24002.

[16] M. J. Cordill, O. Glushko, B. Putz, Electro-Mechanical Testing of Conductive Materials Used in Flexible Electronics 3 (February) (2016) 1–11.

[17] R. Weinberger, Initiation and growth of cracks during desiccation of stratified muddy sediments, Journal of Structural Geology 21 (4) (1999) 379–386.

[18] Z. Qin, N. M. Pugno, M. J. Buehler, Mechanics of fragmentation of crocodile skin and other thin films, Scientific Reports 4 (2014) 1–7.

[19] C.-M. Aldea, S. P. Shah, A. Karr, Effect of Microcracking on Durability of High-Strength Concrete, Transportation Research Record: Journal of the Transportation Research Board 1668 (1) (1999) 86–90.

[20] T. Rev, M. Jalalvand, J. Fuller, M. R. Wisnom, G. Czél, A simple and robust approach for visual overload indication - UD thin-ply hybrid composite sensors, Composites Part A: Applied Science and Manufacturing (2019).

[21] A. Mielke, A Mathematical Framework for Generalized Standard Materials in the Rate-Independent Case, in: R. Helmig, A. Mielke, B. Wohlmuth (Eds.), Multifield Problems in Solid and Fluid Mechanics, Vol. 28 of Lecture Notes in Applied and Computational Mechanics, Springer Berlin / Heidelberg, 2006, pp. 399–428.

[22] A. Mielke, T. Roubíček, Rate-Independent Systems: Theory and Application, Springer, 2015.

[23] R. Alessi, Energetic formulation for rate-independent processes: remarks on discontinuous evolutions with a simple example, Acta Mechanica 227 (10) (2016) 2805–2829.

[24] M. Ambati, T. Gerasimov, L. De Lorenzis, A review on phase-field models of brittle fracture and a new fast hybrid formulation, Computational Mechanics 55 (2015) 383–405.

[25] J.-J. Marigo, C. Maurini, K. Pham, An overview of the modelling of fracture by gradient damage models, Meccanica 51 (12) (2016) 3107–3128.

[26] D. T. Le, J.-J. Marigo, C. Maurini, S. Vidoli, Strain-gradient vs damage-gradient regularizations of softening damage models, Computer Methods in Applied Mechanics and Engineering 340 (2018) 424–450.

[27] G. Lancioni, G. Royer-Carfagni, The Variational Approach to Fracture Mechanics. A Practical Application to the French Panthéon in Paris, Journal of Elasticity 95 (1-2) (2009) 1–30.

[28] F. Freddi, F. Iurlano, Numerical insight of a variational smeared approach to cohesive fracture, Journal of the Mechanics and Physics of Solids 98 (2017) 156–171.

[29] A. Chambolle, V. Crismale, Phase-field approximation for a class of cohesive fracture energies with an activation threshold (dec 2018). arXiv:1812.05301.

[30] V. Crismale, G. Lazzaroni, G. Orlando, Cohesive fracture with irreversibility: quasistatic evolution for a model subject to fatigue, Mathematical Models and Methods in Applied Sciences 28 (2018) 1371–1412.

[31] S. Teichtmeister, D. Kienle, F. Aldakheel, M.-A. Keip, Phase field modeling of fracture in anisotropic brittle solids, International Journal of Non-Linear Mechanics (2017).

[32] B. Li, C. Peco, D. Millán, I. Arias, M. Arroyo, Phase-field modeling and simulation of fracture in brittle materials with strongly anisotropic surface energy, International Journal for Numerical Methods in Engineering 102 (3-4) (2015) 711–727.

[33] G. Lancioni, T. Yalçinkaya, A. Cocks, Energy-based non-local plasticity models for deformation patterning, localization and fracture, Proceedings of the Royal Society A: Mathematical, Physical and Engineering Science 471 (2180) (jul 2015).

[34] C. Miehe, S. Teichtmeister, F. Aldakheel, Phase-field modelling of ductile fracture: a variational gradient-extended plasticity-damage theory and its micromorphic regularization., Philosophical transactions. Series A, Mathematical, physical, and engineering sciences 374 (2066) (apr 2016).

[35] R. Alessi, J.-J. Marigo, C. Maurini, S. Vidoli, Coupling damage and plasticity for a phase-field regularisation of brittle, cohesive and ductile fracture: One-dimensional examples, International Journal of Mechanical Sciences 149 (2018) 559–576.

[36] P. Rodriguez, J. Ulloa, C. Samaniego, E. Samaniego, A variational approach to the phase field modeling of brittle and ductile fracture, International Journal of Mechanical Sciences 144 (2018) 502–517.

[37] R. Alessi, D. Bernardini, Analysis of localization phenomena in Shape Memory Alloys bars by a variational approach, International Journal of Solids and Structures 73-74 (2015) 113–133.

[38] A. A. León Baldelli, C. Maurini, K. Pham, A gradient approach for the macroscopic modeling of superelasticity in softening shape memory alloys, International Journal of Solids and Structures 52 (2015) 45–55.

[39] A. Mielke, T. Roubíček, Numerical approaches to rate-independent processes and applications in inelasticity, ESAIM: Mathematical Modelling and Numerical Analysis 43 (3) (2009) 399–428.

[40] G. Lancioni, V. Corinaldesi, Variational modelling of diffused and localized damage with applications to fiber-reinforced concretes, Meccanica 53 (3) (2018) 531–551.

[41] G. Del Piero, G. Lancioni, R. March, A diffuse cohesive energy approach to fracture and plasticity: the one-dimensional case, Journal of Mechanics of Materials and Structures 8 (2-4) (2013) 109–151.

[42] K. Pham, J.-J. Marigo, From the onset of damage to rupture: construction of responses with damage localization for a general class of gradient damage models, Continuum Mechanics and Thermodynamics 25 (2) (2011) 147–171.

[43] G. Lancioni, Modeling the Response of Tensile Steel Bars by Means of Incremental Energy Minimization, Journal of Elasticity 121 (1) (2015) 25–54.

[44] A. A. León Baldelli, J. F. Babadjian, B. Bourdin, D. Henao, C. Maurini, A variational model for fracture and debonding of thin films under in-plane loadings, Journal of the Mechanics and Physics of Solids 70 (2014) 320–348.

[45] R. Alessi, F. Freddi, Phase-field modelling of failure in hybrid laminates, Composite Structures In press (2017) 9–25.

[46] J. Bleyer, Multiphase continuum models for fiber-reinforced materials, Journal of the Mechanics and Physics of Solids (2018).

[47] E. C. Aifantis, The physics of plastic deformation, International Journal of Plasticity 3 (3) (1987) 211–247.

[48] H.-B. Mühlhaus, E. C. Aifantis, A variational principle for gradient plasticity, International Journal of Solids and Structures 28 (7) (1991) 845–857.

[49] B. A. Graybeal, F. Baby, Development of Direct Tension Test Method for Ultra-High-Performance Fiber-Reinforced Concrete., ACI Materials Journal (110) (2013) 177–186.

[50] J.-I. Choi, B. Y. Lee, R. Ranade, V. C. Li, Y. Lee, Ultra-high-ductile behavior of a polyethylene fiber-reinforced alkali-activated slag-based composite, Cement and Concrete Composites 70 (April) (2016) 153–158.

[51] J.-i. Choi, S. Y. Jang, S.-j. Kwon, B. Y. Lee, Tensile Behavior and Cracking Pattern of an Ultra-High Performance Mortar Reinforced by Polyethylene Fiber 2017 (2017).

[52] S. He, J. Qiu, J. Li, E. H. Yang, Strain hardening ultra-high performance concrete (SHUHPC) incorporating CNF-coated polyethylene fibers, Cement and Concrete Research 98 (April) (2017) 50–60.

[53] V. C. Li, H. Stang, H. Krenchel, Micromechanics of crack bridging in fiber reinforced concrete, Materials and Structures, 26 (1993) 486–494.

[54] J. Y. Wang, J. Y. Guo, Damage investigation of ultra high performance concrete under direct tensile test using acoustic emission techniques, Cement and Concrete Composites 88 (2018) 17–28.

[55] A. Braides, A. Causin, M. Solci, A homogenization result for interacting elastic and brittle media, Proceedings of the Royal Society A: Mathematical, Physical and Engineering Science 474 (2218) (2018) 20180118.

[56] R. Alessi, J.-J. Marigo, S. Vidoli, Gradient damage models coupled with plasticity: Variational formulation and main properties, Mechanics of Materials 80 (Part B) (2015) 351–367.

[57] P. Gudmundson, A unified treatment of strain gradient plasticity, Journal of the Mechanics and Physics of Solids 52 (6) (2004) 1379–1406.

[58] M. E. Gurtin, L. Anand, Thermodynamics applied to gradient theories involving the accumulated plastic strain: The theories of Aifantis and Fleck and Hutchinson and their generalization, Journal of the Mechanics and Physics of Solids 57 (3) (2009) 405–421.

[59] M. E. Gurtin, E. Fried, L. Anand, The mechanics and thermodynamics of continua, Cambridge University Press, Cambridge, 2010.

[60] J. Ulloa, P. Rodríguez, E. Samaniego, On the modeling of dissipative mechanisms in a ductile softening bar, Journal of Mechanics of Materials and Structures 11 (4) (2016) 463–490.

[61] J. Jungwirth, A. Muttoni, Structural behavior of tension members in UHPC, Proceeding of International Symposium on UHPC (2004) 1–12.

[62] R. Alessi, J. Ciambella, A. Paolone, Damage evolution and debonding in hybrid laminates with a cohesive interfacial law, Meccanica 52 (4-5) (2017) 1079–1091.

[63] C. A. Nonato Da Silva, J. Ciambella, J. A. O. Barros, I. G. Costa, Analytical bond model for general type of reinforcements of finite embedment length in cracked cement based materials, International Journal of Solids and Structures 167 (2019) 36–47.